

**Solubility of the hydrated Mg-carbonates nesquehonite and dypingite from 5 to 35°C:  
Implications for CO<sub>2</sub> storage and the relative stability of Mg-carbonates**

Anna L. Harrison<sup>a,b,1\*</sup>, Vasileios Mavromatis<sup>b,c</sup>, Eric H. Oelkers<sup>a,b</sup>, and Pascale Bénézech<sup>b</sup>

<sup>a</sup>Department of Earth Sciences, University College London, Gower Street, WC1E 6BT  
London, United Kingdom (anna.harrison@ucl.ac.uk; e.oelkers@ucl.ac.uk)

<sup>b</sup>Geoscience and Environment Toulouse (GET), CNRS, UMR 5563, Observatoire Midi-  
Pyrénées, 14 Avenue Edouard Belin, 31400 Toulouse, France

(vasileios.mavromatis@get.omp.eu; [eric.oelkers@get.omp.eu](mailto:eric.oelkers@get.omp.eu); [pascale.benezeth@get.omp.eu](mailto:pascale.benezeth@get.omp.eu))

<sup>c</sup>Institute of Applied Geosciences, Graz University of Technology, Rechbauerstrasse 12,  
8010 Graz, Austria

<sup>1</sup>Present address: Department of Geological Sciences and Geological Engineering and School  
of Environmental Studies, Queen's University, K7L 3N6 Kingston, Canada

\*Corresponding author: [anna.harrison@queensu.ca](mailto:anna.harrison@queensu.ca)

## 1 **Abstract**

2 Hydrated Mg-carbonate minerals form during the weathering of ultramafic rocks, and  
3 can be used to sequester atmospheric CO<sub>2</sub> to help combat greenhouse gas-fueled climate  
4 change. Optimization of engineered CO<sub>2</sub> sequestration and prediction of the composition and  
5 stability of Mg-carbonate phase assemblages in natural and engineered ultramafic  
6 environments requires knowledge of the solubility of hydrated Mg-carbonate phases, and the  
7 transformation pathways between these metastable phases. In this study, we evaluate the  
8 solubility of nesquehonite [MgCO<sub>3</sub>·3H<sub>2</sub>O] and dypingite [Mg<sub>5</sub>(CO<sub>3</sub>)<sub>4</sub>(OH)<sub>2</sub>·(5 or 8)H<sub>2</sub>O] and  
9 the transformation from nesquehonite to dypingite between 5°C and 35°C, using constant-  
10 temperature, batch-reactor experimentals.. The logarithm of the solubility product of  
11 nesquehonite was determined to be: -5.03±0.13, -5.27±0.15, and -5.34±0.04 at 5°C, 25°C,  
12 and 35°C, respectively. The logarithm of the solubility product of dypingite, never reported  
13 before, was determined to be: -34.95±0.58 and -36.04±0.31 at 25°C and 35°C, respectively,  
14 with eight waters of hydration. The transformation from nesquehonite to dypingite was  
15 temperature-dependent, and was complete within 57 days at 25°C, and 20 days at 35°C, but  
16 did not occur during experiments of 59 days at 5°C. This phase transformation appeared to  
17 occur via a dissolution-reprecipitation mechanism; external nesquehonite crystal morphology  
18 was partially maintained during the phase transformation at 25°C, but was eradicated at 35°C.  
19 Together, our results facilitate the improved evaluation of Mg-carbonate mineral precipitation  
20 during natural and engineered ultramafic mineral weathering systems that sequester CO<sub>2</sub>, and  
21 for the first time allow assessment of the saturation state of dypingite in aqueous solutions.

22

23 **Keywords:** Mg-carbonates; CO<sub>2</sub> sequestration; mineral solubility; ultramafic mineral  
24 weathering; mineral phase transformation; dissolution-reprecipitation; dypingite;  
25 nesquehonite

## 26 **1. Introduction**

27

28         The largest proportion of carbon on Earth's crust is bound in carbonate minerals,  
29 where it is stable over millennia (Sundquist, 1993; Lackner, 2003). The engineered storage of  
30 anthropogenic CO<sub>2</sub> in carbonate minerals is therefore sought to offset greenhouse gas  
31 emissions and mitigate climate change (Lackner et al., 1995; Kelemen and Matter, 2008;  
32 Oelkers and Cole, 2008; Power et al., 2013a, b; Matter et al., 2016). Carbonate mineral  
33 formation during the weathering of silicates and hydroxides is a naturally occurring process,  
34 known as carbon mineralization; this process can be enhanced artificially to sequester CO<sub>2</sub>.  
35 Several engineered carbon mineralization approaches have been studied at the laboratory  
36 and/or pilot-scale, including injection of CO<sub>2</sub> into subsurface basaltic or ultramafic rock  
37 (Kelemen and Matter, 2008; Power et al., 2013a, b; Gislason and Oelkers, 2014; Matter et al.,  
38 2016), passive or accelerated carbonation of ultramafic mine waste rock and tailings (Wilson  
39 et al., 2006, 2009, 2011, 2014; Power et al., 2010, 2014a; Pronost et al., 2011, 2012; Bea et  
40 al., 2012; Beinlich and Austrheim, 2012; Harrison et al., 2013a, b, 2015, 2016; Oskierski et  
41 al., 2013; Assima et al., 2012, 2014a, b, c; McCutcheon et al., 2015, 2017; Gras et al., 2017),  
42 and accelerated mineralization in high pressure/high temperature *ex situ* reactors (Lackner et  
43 al., 1995; Gerdemann et al., 2007). Enhanced weathering is a related approach that aims  
44 primarily to sequester CO<sub>2</sub> in dissolved form, but can also induce carbonate precipitation. It  
45 entails spreading fine-grained mafic or ultramafic rock in natural weathering environments to  
46 artificially enhance natural weathering (Schuiling and Boer, 2010; Renforth, 2012; Hartmann  
47 et al., 2013; Montserrat et al., 2017; Rigopoulos et al., 2018). Estimation of the CO<sub>2</sub> storage  
48 security of these approaches requires knowledge of the stability, solubility, and formation  
49 pathways of the carbonate mineral products that store the CO<sub>2</sub>. The relative stability and  
50 solubility of several Mg-carbonates has been investigated (Langmuir, 1965; Canterford et al.,

51 1984; Königsberger et al., 1999; Zhang et al., 2006; Hopkinson et al., 2008, 2012; Hänchen  
52 et al., 2008; Xiong and Lord, 2008; Bénézeth et al., 2011; 2018; Xiong, 2011; Ballirano et al.,  
53 2013; Berninger et al., 2014; Kristova et al., 2014; Gautier et al., 2014). In general, the  
54 stability of Mg-carbonates increases from more to less hydrated phases, in the order:  
55 lansfordite < nesquehonite < dypingite < hydromagnesite < magnesite (Langmuir, 1965;  
56 Canterford et al., 1984). Due to the strong hydration of aqueous Mg, the formation of  
57 anhydrous magnesite [MgCO<sub>3</sub>], is kinetically inhibited at low temperatures, and is rarely  
58 observed to form on laboratory timescales at temperature less than 60°C (Hänchen et al.,  
59 2008; Saldi et al., 2009, 2012; Power et al., 2017). For example, Gautier et al. (2014)  
60 demonstrate a 2.5-fold greater growth rate constant for hydromagnesite  
61 [Mg<sub>5</sub>(CO<sub>3</sub>)<sub>4</sub>(OH)<sub>2</sub>·4H<sub>2</sub>O] compared to magnesite at 90°C. Thus, ultramafic weathering at the  
62 Earth's near-surface is dominated by hydrated Mg-carbonate formation (Shirokova et al.,  
63 2013; Power et al., 2014b; Lin et al., 2017), and engineered CO<sub>2</sub> sequestration efforts at near-  
64 Earth's surface temperatures will also tend to form hydrated Mg-carbonates. However,  
65 observed mineral assemblages in the field and in laboratory experiments reveal that multiple  
66 hydrated magnesium carbonate phases often co-exist, with the more-hydrated phases  
67 frequently acting as transient precursors to the more stable, less-hydrated phases (Davies and  
68 Bubela, 1973; Hopkinson et al., 2008, 2012; Wilson et al., 2009; Ballirano et al., 2013; Power  
69 et al., 2014b; Harrison et al., 2015, 2016). The multitude of potential metastable hydrated  
70 phases complicates prediction of Mg-carbonate formation and thus the stability of the CO<sub>2</sub>-  
71 storing phase (Königsberger et al., 1999; Hopkinson et al., 2008, 2012; Hänchen et al., 2008;  
72 Montes-Hernandez et al., 2012; Kristova et al., 2014). To reduce some of the ambiguity in  
73 the prediction of Mg-carbonate mineral formation under various conditions, in this study we  
74 determine the solubility of nesquehonite [MgCO<sub>3</sub>·3H<sub>2</sub>O] and dypingite [Mg<sub>5</sub>(CO<sub>3</sub>)<sub>4</sub>(OH)<sub>2</sub>·(5  
75 or)8H<sub>2</sub>O], two commonly observed products of carbon mineralization in ultramafic materials

76 (Wilson et al., 2006, 2009, 2011, 2014; Boschi et al., 2009; Zhao et al., 2010; Pronost et al.,  
77 2011; Schaef et al., 2011; Bea et al., 2012; Loring et al., 2012; Montes-Hernandez et al., 2012;  
78 Assima et al., 2012, 2014c; Hövelmann et al., 2012; Felmy et al., 2012; Beinlich and  
79 Austrheim, 2012; Schaef et al., 2013; Harrison et al., 2013a, 2015, 2016, 2017; Power et al.,  
80 2013a, b, c, 2014b; Kristova et al., 2014; McCutcheon et al., 2016; Chaka et al., 2016; Garcia  
81 del Real et al., 2016; Highfield et al., 2016; Gras et al., 2017; McCutcheon et al., 2017), and  
82 the transformation process that converts nesquehonite to dypingite. Both nesquehonite and  
83 dypingite are readily formed during reaction of Mg-rich minerals with CO<sub>2</sub> at ambient  
84 temperatures, with nesquehonite tending to form at greater than atmospheric *p*CO<sub>2</sub> or  
85 evaporative conditions (Königsberger et al., 1999; Power et al., 2007; Xiong and Lord, 2008;  
86 Zhao et al., 2010; Schaef et al., 2011; Harrison et al., 2013a), and dypingite favored under  
87 atmospheric *p*CO<sub>2</sub> (~400 ppm) and microbially-mediated conditions (Power et al., 2007;  
88 Wilson et al., 2010; Mavromatis et al., 2012; Shirokova et al., 2013; Harrison et al., 2013a;  
89 McCutcheon et al., 2016). In addition to their natural occurrence and use for CO<sub>2</sub> storage,  
90 hydrated Mg-carbonates have prompted interest due to their potential formation in engineered  
91 Mg(OH)<sub>2</sub>/MgO barriers for nuclear waste storage (Xiong and Lord, 2008; Xiong, 2011), and  
92 the precipitation of nesquehonite from MgCl<sub>2</sub> brines has been investigated as a way to exploit  
93 Mg resources from salt lakes (Dong et al., 2008; Wang et al., 2008; Cheng et al., 2009;  
94 Cheng and Li, 2009), and as a precursor for high purity MgO production (Cheng et al., 2009;  
95 Wang and Li, 2012). This broad interest in nesquehonite has inspired a number of studies  
96 regarding its thermal stability (Lanas and Alvarez, 2004; Hales et al., 2008; Vágvölgyi et al.,  
97 2008; Ballirano et al., 2010; Jauffret et al., 2015; Morgan et al., 2015), nucleation kinetics  
98 (Cheng and Li, 2010; Zhao et al., 2013), its tendency for solid-solution with transition metals  
99 (Hamilton et al., 2016), and the impacts of temperature, saturation state, and fluid  
100 composition on nucleation and crystal morphology and size (Zhang et al., 2006; Wang et al.,

101 2008; Cheng et al., 2009; Ding et al., 2016). Robie and Hemingway (1972; 1973) determined  
102 its standard heat capacity, standard entropy, and standard enthalpy of formation. Although  
103 several solubility studies of nesquehonite have been conducted both experimentally and  
104 theoretically, they report differing results, or in some cases do not report a solubility product,  
105 instead reporting total aqueous Mg or C concentrations (*c.f.*, Kline, 1929; Kazakov et al.,  
106 1959; Hostetler, 1964; Langmuir, 1965; Königsberger et al., 1999; Dong et al., 2008, 2009;  
107 Wang and Li, 2012). On the other hand, dypingite solubility remains undetermined, despite  
108 its common occurrence in natural and engineered ultramafic weathering environments  
109 (Power et al., 2013a and references therein). Dypingite can be a precursor for the formation  
110 of hydromagnesite (Davies and Bubela, 1973; Hopkinson et al., 2008, 2012; Sutradhar et al.,  
111 2011), a mineral that securely stores CO<sub>2</sub> over tens of thousands of years at Earth's surface  
112 conditions (e.g., Power et al., 2009; 2014). The process by which the metastable hydrous Mg-  
113 carbonates transform from less to more stable phases is also an important control on the  
114 isotopic signature of the carbonate minerals, which can be used to trace CO<sub>2</sub> cycling and  
115 sequestration processes (Power et al., 2007, 2014b; Wilson et al., 2009, 2010, 2011, 2014;  
116 Beinlich and Austrheim, 2012; Shirokova et al., 2013; Harrison et al., 2013a, 2016; Oskierski  
117 et al., 2013; Mervine et al., 2014; Falk et al., 2016; Oskierski et al., 2016; Gras et al., 2017).  
118 Similarly, the mobility of toxic metals that can be incorporated in nesquehonite (Hamilton et  
119 al., 2016) will be controlled in part by the efficiency and mechanism of Mg-carbonate phase  
120 transformations.

121         The goals of the present study were to 1) determine the solubility of nesquehonite and  
122 dypingite at conditions relevant to natural and engineered CO<sub>2</sub>-driven weathering, and 2)  
123 assess the nesquehonite-dypingite transformation pathway and the implications for CO<sub>2</sub>  
124 storage.

125

126

## 127 **2. Methods**

128

### 129 *2.1. Nesquehonite and dypingite synthesis*

130 Nesquehonite was synthesized according to a modified method of Robie and  
131 Hemingway (1972), whereby 200 mL of an aqueous 1.8 M  $K_2CO_3$  solution (reagent grade  
132  $K_2CO_3$ ) was slowly added to a 1000 mL glass beaker containing 200 mL of 1.8 M aqueous  
133  $MgCl_2$  (NormaPur  $MgCl_2 \cdot 6H_2O$ ). The beaker was then covered with a watch glass to permit  
134 some exchange with laboratory air but limit evaporation and dust inputs. A white gel-like  
135 precipitate was formed immediately upon mixing of the two solutions. This precipitate was  
136 allowed to age in the solution for five days at ambient temperature ( $\sim 22^\circ C$ ) after which the  
137 slurry was vacuum-filtered and rinsed multiple times with distilled, de-ionized water. The  
138 precipitate was then dried at ambient temperature for  $\sim 3$  days. Once dry, the precipitate was  
139 gently disaggregated using an agate mortar and pestle, and stored in a desiccator prior to  
140 analysis and use in experiments. The nesquehonite was made in two separate batches due to  
141 the large quantity required, and each was used in separate experimental runs; a short-term  
142 experiment (nesquehonite batch 1), and a long-term experiment (nesquehonite batch 2). The  
143 long-term experiment was conducted subsequent to the short-term experiment to capture the  
144 complete conversion of nesquehonite to dypingite. Dypingite was synthesized via  
145 transformation of the synthetic nesquehonite within the experiments. The experimental  
146 conditions are described in more detail in Section 2.2.

147 The synthetic nesquehonite was characterized using X-ray diffraction (XRD) and  
148 Fourier transform infrared spectroscopy (FTIR), which confirmed the presence of only  
149 nesquehonite in the initial solids used in the experiments (Figures 1 and 2). The empirical  
150 formula of nesquehonite has been debated, and is sometimes reported as

151 [Mg(OH)(HCO<sub>3</sub>)·2H<sub>2</sub>O] (Frost and Palmer, 2011). However, the FTIR spectra were more  
152 consistent with the formula [MgCO<sub>3</sub>·3H<sub>2</sub>O], as the bicarbonate-derived band at 985 cm<sup>-1</sup>  
153 (Zhang et al., 2006) was not present (Figure 1). Scanning electron microscopy (SEM) images  
154 (Figure 3) revealed a needle-like morphology typical of nesquehonite (*c.f.*, Power et al., 2009;  
155 Zhao et al., 2010; Schaef et al., 2011; Harrison et al., 2013a, 2017). Neither XRD nor FTIR  
156 data revealed significant differences between the two batches of synthetic nesquehonite  
157 (Figures 1 and 2), though SEM revealed a slightly higher proportion of fine particles in the  
158 second synthesized batch, which was used for the longer-term experiments.

159

## 160 2.2. *Experimental methods*

161 Experiments to determine the solubility product of nesquehonite were conducted at  
162 constant temperatures of 5°C, 25°C, and 35°C. A single experiment was conducted at 5°C,  
163 whereas duplicate experiments were conducted at 25°C and 35°C. The duplicate experiments  
164 ran subsequently to the originals, and for a longer duration, to ensure the complete  
165 conversion of nesquehonite to dypingite. Each experiment consisted of a suite of nine to  
166 eleven sealed, closed system reactors. The starting aqueous solution and solid were first  
167 added to the individual reactors (Nalgene bottles) in identical amounts. Each bottle contained  
168 0.06 g of nesquehonite and ~73.4 g of an aqueous solution containing 0.10 M NaCl and 0.06  
169 M NaHCO<sub>3</sub>. At various selected times, an individual reactor was sampled in its entirety  
170 (liquid and solid). This approach was taken to ensure the solid and its contemporaneous fluid  
171 were collected, and to avoid generation of headspace due to sampling, as would occur by  
172 sampling fluids from a single reactor. The individual reactors were filled with minimal  
173 headspace to inhibit loss of CO<sub>2(g)</sub> from solution. To avoid precipitation due to temperature  
174 changes, the experimental solutions were prepared by first heating or cooling distilled, de-  
175 ionized water (18.2 MΩ cm<sup>-1</sup>) to the desired experimental temperature, followed by the



176 addition of reagent-grade NaCl and NaHCO<sub>3</sub> to reach the desired concentration. This aqueous  
177 solution was then poured into the individual reactors, which already contained nesquehonite,  
178 and the reactors were rapidly sealed, weighed, and placed at the experimental temperature.  
179 Experiments conducted at 5°C were placed on an orbital shaker in a thermostatic refrigerator,  
180 whereas experiments conducted at 25°C and 35°C were conducted in shaking water baths at  
181 constant temperature.

182 Individual reactors were sampled one at the time to track the chemical composition of  
183 the reactive aqueous solution, as well as changes in the mineral composition of the solids.  
184 Upon sampling, reactors were weighed to assess evaporative losses and the solution  
185 temperature was measured using a thermometer. The solution was then removed via a syringe  
186 and needle, and filtered with a 0.22 µm polyethersulfone (PES) syringe filter. Two aliquots  
187 were immediately acidified to 2% HNO<sub>3</sub> for subsequent analysis of Mg concentrations, and a  
188 single aliquot was used for immediate pH measurements, and later alkalinity measurements.  
189 Fluid pH was measured using a Metrohm 913 pH-meter and a Metrohm combined electrode  
190 (6.0234.1000) that was calibrated using NIST traceable pH<sub>25°C</sub> 4.01, 7.00, and 9.18 buffer  
191 solutions at each experimental temperature, with an uncertainty of approximately ±0.03 pH  
192 units. Dissolved inorganic carbon concentration was calculated using PHREEQC V3  
193 (Parkhurst and Appelo, 2013) and a modified LLNL database, based on the measured fluid  
194 compositions. Geochemical modeling methods are discussed in further detail in Section 2.4.

195 The solids were separated from any remaining solution via vacuum filtration, and  
196 were rinsed with distilled, de-ionized water to prevent NaCl precipitation. They were then  
197 dried at room temperature for ~48 h and stored in a desiccator prior to analysis. Note that  
198 hydrated Mg-carbonate minerals must be stored under dry conditions to prevent their  
199 transformation in humid air (Davies and Bubela, 1973; Power et al., 2016), therefore care  
200 was taken to minimize exposure to laboratory air at all times.

201 Dypingite was formed *in situ* within the reactors at 25°C and 35°C, with longer-term  
202 experiments designed to allow the complete transformation from nesquehonite to dypingite  
203 and to capture a period of stable solution chemistry representative of equilibrium between the  
204 dypingite and the reactive aqueous solution. The phase transformation was tracked via  
205 changes in aqueous solution composition and mineralogical data collected using XRD  
206 complemented with FTIR for some samples.

207

### 208 2.3. Analytical techniques

209 The alkalinity of all fluid samples was determined by HCl titration using an  
210 automated Schott Titroline Alpha Plus titrator. Long term reproducibility, determined from  
211 repeated analysis of a standard, was better than  $\pm 0.36 \times 10^{-2}$  mol/L ( $3\sigma$ ), and the detection  
212 limit was  $5 \times 10^{-5}$  mol/L. Dissolved inorganic carbon (DIC) concentrations were calculated  
213 using the measured fluid composition and PHREEQC V3 (Parkhurst and Appelo, 2013) with  
214 a modified LLNL database, as described in further detail in Section 2.4. The uncertainty  
215 introduced via the calculation of DIC is unknown; a minimum uncertainty equal to that of the  
216 alkalinity measurement is assumed ( $\pm 0.36 \times 10^{-2}$  mol/L). Aqueous Mg concentrations were  
217 measured by atomic absorption spectroscopy (AAS) using a Perkin Elmer AAnalyst 400.  
218 Samples and standards were matrix-matched in 0.01 mol/L HNO<sub>3</sub>. All samples were  
219 measured in triplicate and reported concentrations represent averages of these measurements,  
220 the standard deviation ( $3\sigma$ ) is smaller than the symbols employed in figures, unless otherwise  
221 shown. Reproducibility was better than 2%, and the quantification and detection limits were  
222  $2.3 \times 10^{-3}$  ppm and  $7.0 \times 10^{-4}$  ppm, respectively. Quantification and detection limits were  
223 defined as  $10\sigma$  and  $3\sigma$  over background variation.

224 The mineralogical compositions of the solids were determined using powder XRD  
225 with a Bruker D2 Phaser with Cu radiation. The scan speed was 0.5 s/step, and a step size of

226 0.02°/step was used. To complement the XRD data, FTIR analysis was conducted on select  
227 samples using a ThermoScientific Nicolet iN 10 MX infrared imaging microscope.  
228 Morphological characteristics were examined via scanning electron microscopy using a  
229 JEOL JSM 6360LV or a JEOL JSM 6480LV.

230

#### 231 *2.4. Geochemical modeling*

232 The standard state adopted in this study is that of unit activity at any temperature and  
233 pressure for pure minerals. The standard state for aqueous species at any temperature and  
234 pressure is unit activity of a hypothetical 1 molal solution referenced to infinite dilution.  
235 Aqueous speciation and mineral saturation states were calculated using PHREEQC V3  
236 (Parkhurst and Appelo, 2013) and its LLNL database, which was modified to include the  
237 carbonic acid dissociation constants of Patterson et al. (1982; 1984), the  $\text{Mg}^{2+}$  hydrolysis  
238 constant from Palmer and Wesolowski (1997), the formation constants of  $\text{MgHCO}_3^+$  and  
239  $\text{MgCO}_3^\circ$  ion pairs from Stefansson et al. (2014), the magnesite solubility product from  
240 Bénézeth et al. (2011), the hydromagnesite solubility product from Gautier et al. (2014), and  
241 the brucite solubility product from Brown et al. (1996). Activity coefficients are calculated  
242 using the b-dot model (Helgeson, 1969).

243

### 244 **3. Results**

#### 245 *3.1 Phase transformations*

##### 246 *3.1.1 Phase transformation at 25°C*

247 The measured Mg concentration, pH, alkalinity, mineralogical composition, the  
248 calculated DIC concentration, and determined aqueous  $\text{Mg}^{2+}$ ,  $\text{CO}_3^{2-}$ , and  $\text{H}_2\text{O}$  activities with  
249 time in all experiments are listed in Table 1. At 5°C, nesquehonite did not transform into a  
250 different phase throughout the 1420 h (59 d) experiment as confirmed by XRD (Electronic

251 Supplement (ES) -Figure 1). Similarly, SEM micrographs revealed that the solid phase  
252 maintained the needle-like nesquehonite morphology throughout the experiment (Figure 3).

253 At 25°C, minor dypingite was first detected with XRD at 359 h in the long-term  
254 experiment, and dypingite formed between 367 h and 1086 h during the short-term  
255 experiment (ES-Figures 2 and 3). Trace dypingite was also detected in the 22 h sample in the  
256 long-term 25°C experiment, however, the lack of change in solution composition at this time,  
257 its non-existence in the solids collected from the subsequent sample, and the lack of  
258 dypingite over this timeframe in the short-term 25°C experiment suggest that its presence in  
259 the 22 h sample from the long-term experiment is an artifact of improper sample storage, not  
260 dypingite formation in the experiment. The sample collected at 359 h in the long-term  
261 experiment exhibits particles with needle-like external morphology, similar to the initial  
262 nesquehonite, but with rounded edges, and a flakey, porous surface (Figure 3c). This flakey  
263 morphology is typical of dypingite (e.g., Canterford et al., 1984; Power et al., 2007;  
264 Mavromatis et al., 2012), and suggests the precipitation of dypingite is closely coupled to the  
265 dissolution of nesquehonite at the mineral-fluid interface, as has been observed for several  
266 mineral replacement reactions (e.g., Ruiz-Agudo et al., 2012 and references therein). Within  
267 1367 h, nesquehonite was completely replaced by dypingite, and no other phase was  
268 observed for the remainder of the 2043 h (85 d) long-term experiment (ES-Figure 3).

269 Dypingite is normally reported in the literature to have the chemical formula  
270  $[\text{Mg}_5(\text{CO}_3)_4(\text{OH})_2 \cdot 5\text{H}_2\text{O}]$ , but has also been reported to have the formula  
271  $[\text{Mg}_5(\text{CO}_3)_4(\text{OH})_2 \cdot 8\text{H}_2\text{O}]$ , and more rarely  $[\text{Mg}_5(\text{CO}_3)_4(\text{OH})_2 \cdot 6\text{H}_2\text{O}]$  (Raade, 1970;  
272 Canterford et al., 1984; Xiong and Lord, 2008; Hopkinson et al., 2012; Kristova et al., 2014).

273 The XRD pattern of the dypingite in our experiments was consistent with  
274  $[\text{Mg}_5(\text{CO}_3)_4(\text{OH})_2 \cdot 8\text{H}_2\text{O}]$  (International center for diffraction data, pattern PDF-00-029-  
275 0857; ES-Figures 3-5), which differs from that of  $[\text{Mg}_5(\text{CO}_3)_4(\text{OH})_2 \cdot 5\text{H}_2\text{O}]$  (International

276 center for diffraction data, pattern PDF-00-023-1218), by the presence of a low angle peak at  
277  $2.659^\circ 2\theta$  ( $d = 33.200$ ). Other than this peak, the similarity of the XRD patterns for dypingite  
278 with 5 or 8 hydration waters means the presence of  $[\text{Mg}_5(\text{CO}_3)_4(\text{OH})_2 \cdot 5\text{H}_2\text{O}]$  in addition to  
279  $[\text{Mg}_5(\text{CO}_3)_4(\text{OH})_2 \cdot 8\text{H}_2\text{O}]$  cannot be excluded.

280 An additional phase was observed in the long-term experiment from 599 h until the  
281 end of the experiment; this additional phase is characterized by two small, low-angle peaks  
282 (labeled “d-1” in ES-Figure 3). Dypingite-like phases with varying degrees of hydration and  
283 similar structures, which exhibit low-angle XRD peaks, have been observed in several studies  
284 (Davies and Bubela, 1973; Hopkinson et al., 2008; Hopkinson et al., 2012; Ballirano et al.,  
285 2013; Kristova et al., 2014). For example, during the degassing of a Mg-CO<sub>3</sub> solution at 58°C,  
286 Hopkinson et al. (2012) observed what they referred to as several “dypingite-type” phases  
287 with similar crystal structures but different cell volumes and varying numbers of waters of  
288 hydration, including  $[\text{Mg}_5(\text{CO}_3)_4(\text{OH})_2 \cdot 8\text{H}_2\text{O}]$ . Additional peaks not reported in the  
289 established dypingite XRD patterns were also observed at  $\sim 3.5^\circ$  and  $\sim 6^\circ$  by Ballirano et al.  
290 (2013) during the phase transformation of nesquehonite at room temperature. These low  
291 angle peaks and their inconsistent appearance are attributed to the large and varied cell-  
292 volume of dypingite-like phases, different stacking-sequences of the layers of MgO<sub>6</sub> and  
293 carbonate groups, or different water contents (Ballirano et al., 2013). As such, the low angle  
294 peaks observed from 599 h until the end of the experiment, are attributed to an additional  
295 dypingite-like phase, potentially differing in cell volume and/or number of hydration waters.  
296 To further evaluate the dypingite-like phase documented at 25°C, the FTIR spectrum of a  
297 sample containing this phase (25°C, 1607 h) was compared to the FTIR spectrum of a sample  
298 from the long-term 35°C experiment, which contained only XRD-identifiable dypingite  
299 (35°C, 560 h). The FTIR spectra are close to identical (Figure 1), consistent with the

300 interpretation that the unnamed phase documented in the 25°C experiments is likely another  
301 dypingite-like phase.

302 Changes in fluid composition were coincident with the phase transformation  
303 documented with XRD. During the phase transformation, pH decreased from ~9.2 to ~8.8  
304 between 120 h and 599 h before stabilizing at ~8.8 for the remainder of the experiment  
305 (Figures 4a and 4d). This suggests that the phase transformation consumes protons despite  
306 forming a hydroxyl-bearing phase. The Mg concentration exhibited a minor decrease during  
307 the phase transformation (Figures 4b and 4e), whereas the DIC exhibited a slight increase  
308 (Figures 4c and 4f). After 599 h, DIC and Mg concentration again remained stable for the  
309 remainder of the experiment (Figures 4b and 4c).

310

### 311 3.1.2. Phase transformation at 35°C

312 At 35°C, the transformation from nesquehonite to dypingite was more rapid than at  
313 25°C. Dypingite was first detected at trace levels by XRD in the 75 h sample from the short-  
314 term experiment (ES-Figure 4), and in the 123 h sample from the long-term experiment (ES-  
315 Figure 5). Similar to the 25°C experiment, the dypingite XRD pattern was consistent with  
316 that of  $[\text{Mg}_5(\text{CO}_3)_4(\text{OH})_2 \cdot 8\text{H}_2\text{O}]$  (International center for diffraction data, pattern PDF-00-  
317 029-0857; ES-Figures 4 and 5). The additional dypingite-like phase observed at 25°C was not  
318 evident in the 35°C experiments, however, a different unidentified phase was recorded in the  
319 sample at 718 h in the long-term experiment (identified as “unknown” in ES-Figure 5),  
320 evidenced by additional peaks at ~27° and ~33° and the disappearance of the ~11° peak. It is  
321 not clear whether this was an additional phase, or representative of a change in the dypingite  
322 structure. This phase was not present before or after 718 h, nor was it traced in the short-term  
323 experiment. It may be an artifact of imperfect sample storage, rather than reflecting an *in situ*  
324 mineralogical change in the reactors. However, if it was the case, that would affect solubility

325 calculations. In doubt, this sample was not included in calculation of the solubility product.  
326 Nesquehonite was no longer present within 482 h at 35°C (ES-Figure 5), compared to 1367 h  
327 for complete conversion of nesquehonite at 25°C.

328 SEM images revealed a different evolution of crystal morphology between the 25°C  
329 and 35°C experiments; unlike at 25°C, the external crystal morphology of nesquehonite was  
330 not maintained. Rather, over a similar time-frame, the needle-like morphology was replaced  
331 by flakey aggregates with typical dypingite morphology (Figure 3d) (*e.g.*, Canterford et al.,  
332 1984; Power et al., 2007; Mavromatis et al., 2012). This difference in morphological  
333 evolution may be a consequence of the different reaction rates. In both cases, the morphology  
334 change suggests the mineral phase transformation occurs via dissolution-reprecipitation.  
335 However, the slower rate of nesquehonite dissolution at 25°C coupled to the rapid re-  
336 precipitation as dypingite could result in the observed pseudo-morphic replacement at this  
337 temperature. Conversely, a relatively high nesquehonite dissolution rate compared to  
338 dypingite precipitation rate at 35°C, would allow a spatial and thus morphological separation  
339 of the two phases.

340 Similar to the fluid composition change observed during the phase transformation at  
341 25°C, the pH, Mg concentration, and DIC concentration evolved during the nesquehonite-  
342 dypingite transformation at 35°C (Figure 4). A decrease in pH from ~9.15 to ~8.66 occurred  
343 between ~74 h and 482 h (Figures 4a and 4d), while a slight decline in Mg concentration was  
344 observed after 310 h (Figures 4b and 4e). The decline in Mg concentration occurred when the  
345 solids became dominated by dypingite, rather than by nesquehonite (Table 1). A slight  
346 decrease in Mg concentration continued for the remainder of the 35°C experiment, suggesting  
347 either a slow approach to dypingite equilibrium, or perhaps the beginning of a transformation  
348 to a less hydrated Mg-carbonate, though no further mineralogical changes were detected with  
349 XRD or FTIR. A minor increase in DIC concentration was observed after 75 h (Figures 4c

350 and 4f), but DIC was again constant from ~243 h to the end of the short- and long-term  
351 experiments. The short-term experiments were too brief for completion of the nesquehonite-  
352 dypingite transformation, but the trends in fluid composition were consistent with the early  
353 stages of the transformation documented in the longer-term experiments.

354

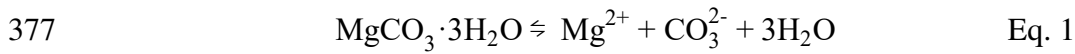
### 355 *3.2 Retrieval of the nesquehonite solubility product*

356 The dissolution of nesquehonite to a constant fluid composition was rapid in all  
357 experiments, with pH, Mg, and alkalinity increasing to constant values within 120 h, 24 h,  
358 and 3 h in the 5°C, 25°C, and 35°C experiments, respectively (Table 1; Figure 4). The values  
359 used for the calculation of nesquehonite and dypingite solubility products at all temperatures  
360 are indicated in Table 1. Brucite [Mg(OH)<sub>2</sub>], which can form at room temperature from Mg-  
361 rich solutions, remained undersaturated in all experiments. Nesquehonite was the only phase  
362 detected with XRD throughout the 5°C experiment (ES-Figure 1), therefore all samples taken  
363 from 120 h, when the fluid composition stabilized, up to the end of the experiment (1420 h)  
364 were included in the calculation of its solubility product ( $K_{sp}^{nsq}$ ). In the 25°C experiment,  
365 nesquehonite was the only phase detectable with XRD for 367 h in the short-term experiment  
366 (ES-Figure 2), though minor dypingite was detected at 359 h in the long-term experiment  
367 (ES-Figure 3). Solution compositions remained constant over these time periods, therefore  
368 samples from between 24 h and 367 h in the short-term experiment, and less than 359 h in the  
369 long-term experiment were used for the calculation of  $K_{sp,25}^{nsq}$ , providing a total of six distinct  
370 points for which the solubility product was calculated and averaged.

371 In the 35°C experiment, the solubility product was calculated using the aqueous  
372 solution composition between 3 h and 24 h in the short-term experiment, and 26 h and 74 h in  
373 the long-term experiment (seven time points in total), representing time points that had  
374 constant fluid composition and no detectable dypingite (Table 1).



375 The nesquehonite solubility product was determined using the average of the  
376 calculated  $Mg^{2+}$  and  $CO_3^{2-}$  aqueous activities according to the reaction



378 and its law of mass action

$$379 \quad K_{sp}^{nsq} = a_{Mg^{2+}} a_{CO_3^{2-}} a_{H_2O}^3 \quad \text{Eq. 2}$$

380

381 The aqueous activities in Eq. 2 were calculated using PHREEQC V3 with the modified  
382 LLNL database, as described in section 2.4, and are listed in Table 1. The nesquehonite  
383 solubility products are reported in Table 2.

384

385

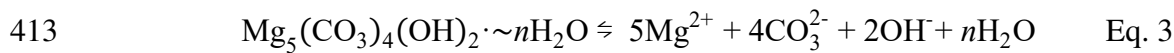
386 Based on the solubility product determined in this study, the standard molar Gibbs  
387 free energy of formation of nesquehonite was also calculated. The standard state properties of  
388 the aqueous species involved in equation 1 were used, and are listed in Table 3. The enthalpy  
389 of the nesquehonite dissolution reaction (equation 1) was estimated by plotting the natural  
390 logarithm of the solubility product versus reciprocal temperature (Figure 5, as shown with  
391 base 10 logarithm), with the slope of the line equated to  $-\Delta H_r^\circ/R$ , where  $\Delta H_r^\circ$  is the enthalpy  
392 of reaction, and  $R$  is the ideal gas constant (Table 3). The standard enthalpy of formation of  
393 nesquehonite was then calculated using the standard state properties of the aqueous species  
394 involved in equation 1, as listed in Table 3.

395

### 396 *3.3 Retrieval of the dypingite solubility product*

397 The solubility product of dypingite ( $K_{sp}^{dyp}$ ) was estimated from the long-term 25°C  
398 and 35°C experiments in which complete transformation to dypingite was achieved.  
399 Dypingite was not formed at 5°C, likely due to slower kinetics of the transformation reaction,

400 thus its solubility product was not determined at this temperature. At 25°C, nesquehonite was  
 401 no longer detected after 1367 h (Table 1; ES-Figure 3), and the fluid composition was  
 402 relatively constant for the remainder of the experiment. This period is therefore taken to  
 403 reflect equilibrium between the dypingite and the aqueous solution, and the solubility product  
 404 was calculated from the final three samples from this experiment (Table 1). At 35°C,  
 405 nesquehonite was no longer detected after 482 h (Table 1; ES-Figure 5); the fluid  
 406 composition also remained relatively constant for the remainder of the experiment. The fluid  
 407 composition from 482 h until the end of the experiment was therefore used to calculate  $K_{sp}^{dyp}$   
 408 (Table 1), except for the sample taken at 718 h, due to the presence of an unidentified phase  
 409 in the solid sample as previously described. A total of five distinct points were used for the  
 410 solubility product calculation at 35°C. Aqueous activities of  $Mg^{2+}$  and  $CO_3^{2-}$  were calculated  
 411 using PHREEQC V3 and the modified LLNL database, and  $OH^-$  activity was calculated from  
 412 pH measurements. The  $K_{sp}^{dyp}$  was calculated using these values and equations 3 and 4.



414

415 
$$K_{sp}^{dyp} = a_{Mg^{2+}}^5 a_{CO_3^{2-}}^4 a_{OH^-}^{-2} a_{H_2O}^n \quad \text{Eq. 4}$$

416 where the variable,  $n$ , was 5 or 8. The presence of at least two dypingite-like phases in the  
 417 25°C experiments, and potentially both  $[Mg_5(CO_3)_4(OH)_2 \cdot 5H_2O]$  and  
 418  $[Mg_5(CO_3)_4(OH)_2 \cdot 8H_2O]$  in the 35°C experiments means that the value calculated for the  
 419 dypingite solubility product likely represents a mixture of dypingite-like phases of varying  
 420 degrees of hydration. Due to the uncertainty in the exact hydration state of dypingite, and the  
 421 presence of an additional dypingite-like phase at 25°C, the  $K_{sp}^{dyp}$  was calculated in three  
 422 ways. Either the activity of water was assumed to be unity, or the activity of water was  
 423 calculated based on the solution composition using PHREEQC V3, and  $K_{sp}^{dyp}$  was

424 determined using eight or five waters of hydration and the aid of equation 4. These are the  
425 most commonly reported stoichiometries for dypingite and have XRD patterns that are  
426 consistent with our experimental data. The  $K_{sp}^{dyp}$  values calculated in each case were  
427 equivalent within error (Table 2), demonstrating that uncertainty in the hydration state of  
428 dypingite does not strongly affect the  $K_{sp}^{dyp}$  retrieved at the experimental ionic strength. The  
429 solubility product (Table 2) decreased slightly with increasing temperature, consistent with  
430 the behavior of nesquehonite (this study) and hydromagnesite  $[\text{Mg}_5(\text{CO}_3)_4(\text{OH})_2 \cdot 4\text{H}_2\text{O}]$   
431 (Gautier et al., 2014).

432

433

#### 434 **4. Discussion**

##### 435 *4.1 Nesquehonite and dypingite solubility products*

436 The standard molar Gibbs free energy of formation of nesquehonite calculated from  
437 our data was in very good agreement with that determined by Robie and Hemingway (1973),  
438 and Langmuir (1965), and the standard molar enthalpy of formation calculated from our data  
439 was in very good agreement with Robie and Hemingway (1973) (Table 3). The nesquehonite  
440 solubility product calculated from our data decreases slightly with increasing temperature,  
441 consistent with the solubility of other Mg- and Ca-carbonate minerals (Table 2) (e.g.,  
442 Königsberger et al., 1999; Marion, 2001; Bénézech et al., 2011, 2018; Gautier et al., 2014),  
443 and temperature dependence reported for nesquehonite solubility in previous studies (Dong et  
444 al., 2008; Wang and Li 2012). However, the temperature dependence is not significant outside  
445  $3\sigma$  uncertainty (Table 2; Figure 5). Our values are in good agreement with those reported in  
446 the modeling study of Wang and Li (2012), which considered the impact of aqueous  
447 speciation on nesquehonite solubility in saline solutions (Table 2). However, discrepancies  
448 are evident between our values and some of the corresponding values at 25°C reported in the

449 literature; values in the present study fall between those of Kline (1929), Langmuir (1965),  
450 and Hostetler (1964) (Table 2; Figure 5); such differences could be attributed to differences  
451 in the calculation of aqueous speciation. The  $\log K_{sp}^{nsq}$  in both the LLNL and minteqv4  
452 PHREEQC databases are most similar to that of Kline (1929), and are considerably larger  
453 than those measured in this study as well as the values reported by Langmuir (1965) and  
454 Hostetler (1964) (Table 2; Figure 5). In addition, the temperature extrapolation employed in  
455 both of these databases exhibits a stronger temperature dependence than that measured in the  
456 present study, or that indicated by Wang and Li (2012) (Figure 5). The neglect of aqueous  
457 speciation in the calculation of the solubility product of Kline (1929) likely explains the  
458 discrepancy between this value and that calculated in our study, as also suggested by  
459 Langmuir (1965) to explain differences between reported nesquehonite solubility products.  
460 The reason for the discrepancy between our measured values and those reported by Hostetler  
461 (1964) and Langmuir (1965) is less clear, but may again relate to differences in the treatment  
462 of aqueous speciation. Robie and Hemingway (1973) suggest that the calorimetric data from  
463 their study are only in agreement with the solubility data of Langmuir (1965) if the aqueous  
464 complexation of Mg by carbonate species assumed by Langmuir (1965) is overestimated.  
465 This could also account for the discrepancy between the Langmuir (1965) value and that  
466 calculated here, but mainly because the present study used recent data for the complexation  
467 of aqueous Mg-carbonate species (Stefansson et al., 2014), which were not available at the  
468 time of the Hostetler (1964) and Langmuir (1965) studies and much of the data regarding  
469 aqueous Mg-carbonate complex stability came after these studies (Stefansson et al., 2014 and  
470 references therein). In addition, the reported stability of  $\text{MgCO}_3^\circ$  and  $\text{MgHCO}_3^+$  aqueous  
471 complexes at 25°C reported in early literature was highly variable (Stefansson et al., 2014). It  
472 is therefore unsurprising that solubility products determined for magnesium carbonates like  
473 nesquehonite differ between studies that used different thermodynamic data for aqueous

474 speciation. The similarity between the Kline (1929) value and those used in the LLNL and  
475 minteqv4 databases suggests they may also lack consideration of aqueous complexation, thus  
476 we propose that values reported in the present study and by Wang and Li (2012) are more  
477 appropriate for calculating nesquehonite saturation state.

478         The dypingite solubility product has not previously been reported, therefore our  
479 calculated  $K_{sp}^{dyp}$  cannot be compared with other dypingite values. Instead, we compare our  
480  $K_{sp}^{dyp}$  values to those of hydromagnesite, a structurally similar but less hydrated Mg-  
481 carbonate. Our calculated  $K_{sp}^{dyp}$  is higher than those reported for hydromagnesite at 25°C:  
482  $K_{sp,25}^{hmg} = 10^{-37.08}$  (Gautier et al., 2014), and  $10^{-41.56}$  (Xiong, 2011), compared to  $K_{sp,25}^{dyp,8H2O} =$   
483  $10^{-34.95 \pm 0.58}$ . This is consistent with previous observations of dypingite behavior, as it is  
484 commonly observed to transform to hydromagnesite over time (Davies and Bubela, 1973;  
485 Hopkinson et al., 2008, 2012; Sutradhar et al., 2011; Ballirano et al., 2013), reflecting its  
486 instability compared to hydromagnesite and therefore its higher solubility product. Using our  
487 dypingite and nesquehonite solubility products, it can be shown that hydromagnesite is more  
488 stable than both of these phases across a broad range of pH and  $pCO_2$  conditions (Figure 6).  
489 However, the relative stability of dypingite and nesquehonite is sensitive to pH for a fixed  
490 DIC concentration (Figure 6). At higher pH there is a greater difference in their relative  
491 stability, with dypingite being more stable than nesquehonite, whereas a smaller difference is  
492 predicted at low pH, owing to the sensitivity of the dypingite solubility product to the activity  
493 of  $OH^-$  (Figure 6).

494

#### 495 *4.2 Implications*

496         Dypingite and nesquehonite are common weathering products of ultramafic rocks  
497 (Wilson et al., 2006, 2009, 2014; Power et al., 2007; Beinlich and Austrheim, 2012; Garcia  
498 del Real et al., 2016; Lin et al., 2017), and are documented  $CO_2$  sinks that can be used to

499 store CO<sub>2</sub> (Power et al., 2007, 2013a, b, c, 2016; Pronost et al., 2011; Bea et al., 2012;  
500 Assima et al., 2012, 2014c ; Harrison et al., 2013a, 2015, 2016, 2017; Wilson et al., 2014;  
501 McCutcheon et al., 2014; Morgan et al., 2015; Hamilton et al., 2016, 2018; Gras et al., 2017).  
502 Yet, a lack of dypingite solubility data has hindered the ability to evaluate and predict its  
503 formation (Power et al., 2007, 2013c, 2014b; Wilson et al., 2010; Mavromatis et al., 2012;  
504 Harrison et al., 2013a; McCutcheon et al., 2014). The results presented in this study allow  
505 better estimation of dypingite stability in aqueous solution. For example, the solubility  
506 products determined in this study were added to PHREEQC V3 and used to calculate the  
507 dypingite saturation state in a previous experimental study in which it formed (Mavromatis et  
508 al., 2012), and in a natural wetland in Atlin, Canada, where it has been observed to form in  
509 microbial mats (Power et al., 2007, 2009, 2014b). In the experimental study (Mavromatis et  
510 al., 2012), dypingite was somewhat supersaturated, suggesting that despite forming more  
511 readily at low temperature than hydromagnesite, its precipitation is nevertheless somewhat  
512 kinetically inhibited (Table 4). In the natural wetlands, where dypingite has both been  
513 directly observed, as well as precipitated in experiments using water from the wetlands  
514 (Power et al., 2007, 2014b), dypingite was very close to equilibrium (Table 4), providing  
515 confidence in our  $K_{sp}^{dyp}$ . The  $K_{sp}^{dyp}$  determined in the present study can therefore be used to  
516 better constrain the possibility of dypingite precipitation in natural environments, and during  
517 engineered CO<sub>2</sub> storage operations. Note also that the nesquehonite solubility products in the  
518 PHREEQC databases appear to underestimate the stability of this mineral compared to the  
519 results of recent studies (this study; Wang and Li, 2012), and may thus underestimate its  
520 likelihood to form.

521         The main goal of engineered CO<sub>2</sub> storage operations is to ensure CO<sub>2</sub> is stored in a  
522 stable form and will not be substantially released over thousand-year timescales. Therefore,  
523 the design of CO<sub>2</sub> storage strategies to produce stable carbonate minerals is a key

524 consideration, and has motivated numerous studies on the relative stability of Mg-carbonate  
525 minerals (Königsberger et al., 1999; Lanas and Alvarez, 2004; Hales et al., 2008; Hopkinson  
526 et al., 2008, 2012; Vágvölgyi et al., 2008; Hänchen et al., 2008; Frost et al., 2008; Ballirano  
527 et al., 2010; Ballirano et al., 2013; Kristova et al., 2014; Jauffret et al., 2015; Morgan et al.,  
528 2015). The stoichiometry of minerals in terms of their Mg:C ratios and Mg:H<sub>2</sub>O ratios also  
529 governs the efficiency of CO<sub>2</sub> sequestration; a Mg:C of 1:1 such as provided by nesquehonite,  
530 lansfordite [MgCO<sub>3</sub> · 5H<sub>2</sub>O], and magnesite is most efficient. In dry conditions, such as in  
531 subaerially stored ultramafic mining wastes (Bea et al., 2012; Wilson et al., 2014), or near the  
532 injection of supercritical CO<sub>2</sub> in the subsurface (Schaefer et al., 2011, 2013; Chaka et al., 2016),  
533 the availability of water may be a limiting factor for carbonate precipitation (Schaefer et al.,  
534 2011, 2013; Harrison et al., 2015, 2016), therefore carbonates that consume less water during  
535 their formation, such as dypingite, hydromagnesite, and magnesite, are desirable. The  
536 anhydrous carbonate, magnesite, is the ideal carbon sink in terms of stability, water  
537 requirements, and efficiency (Power et al., 2017). However, as it does not tend to form at low  
538 temperatures (Hänchen et al., 2008; Saldi et al., 2012), the hydrated carbonates are the targets  
539 for near Earth's surface temperature carbon storage. Although nesquehonite tends to  
540 precipitate from CO<sub>2</sub>-rich solutions and under evaporative conditions (Königsberger et al.,  
541 1999; Power et al., 2007; Zhao et al., 2010; Harrison et al., 2013a), it readily transforms on  
542 hour- to month-long time scales to either dypingite or hydromagnesite, depending on the  
543 temperature. This transformation is accompanied by a slight loss of CO<sub>2</sub> to solution, as  
544 documented in the experiments at 25°C and 35°C (Figure 4c and 4f), which is less ideal for  
545 CO<sub>2</sub> storage. On the other hand, the transformation from dypingite to the more stable phase,  
546 hydromagnesite, does not result in a loss of CO<sub>2</sub> (Ballirano et al., 2013), therefore this  
547 mineral phase transformation minimizes loss of stored CO<sub>2</sub>. This suggests dypingite is a good  
548 target mineral for CO<sub>2</sub> sequestration at low temperatures. The tendency for dypingite to form

549 over nesquehonite at atmospheric  $p\text{CO}_2$  (~400 ppm), suggests that air capture coupled with  
550 carbonate mineral precipitation inherently produces a  $\text{CO}_2$  sink of higher stability, though the  
551 relatively low concentration of  $\text{CO}_2$  in ambient air compared to  $\text{CO}_2$  point sources means that  
552 carbon mineralization rates can be limited by the availability of  $\text{CO}_2$  (Wilson et al., 2010; Bea  
553 et al., 2012; Pronost et al., 2012; Harrison et al., 2013b; Wilson et al., 2014). Microbially-  
554 mediated carbonate precipitation also tends to favor dypingite precipitation (Power et al.,  
555 2007; Mavromatis et al., 2012; McCutcheon et al., 2016), highlighting that microbially-  
556 mediated carbonation is a highly promising strategy for carbon mineralization at near Earth's  
557 surface conditions.

558         Ultramafic rock such as serpentinite contributes disproportionately to the release of  
559 chromium globally during natural weathering processes compared to other rock-types, owing  
560 to its high reactivity and high chromium content (McClain and Maher, 2016; Beinlich et al.,  
561 2018). It has recently been observed that secondary Mg-carbonate minerals formed during the  
562 weathering of ultramafic rock can help to mitigate the release of metals such as chromium,  
563 due both to incorporation of the metals into the carbonate minerals, and trapping of  
564 particulates within carbonate cement (Hamilton et al., 2016; Hamilton et al., 2018). The  
565 relative stability and mechanism of phase transformations is highly relevant to the cycling of  
566 potential contaminants like chromium in both natural and engineered ultramafic weathering  
567 environments. The change in mineral structure between nesquehonite and dypingite, and the  
568 alteration of crystal morphology during the phase transformation is indicative of a  
569 dissolution-reprecipitation process. This implies that metals initially stored in nesquehonite  
570 may be released to solution, and may or may not be equally reincorporated into dypingite,  
571 depending on the relative affinity for metals between the two phases. Similarly, isotopic  
572 signatures, which can be used as tracers for  $\text{CO}_2$  cycling in natural ultramafic environments  
573 and mine wastes (Power et al., 2007; Wilson et al., 2009, 2010, 2011, 2014; Beinlich and



574 Austrheim, 2012; Shirokova et al., 2013; Harrison et al., 2013a, 2016; Oskierski et al., 2013,  
575 2016; Mervine et al., 2014; Mavromatis et al., 2015; Falk et al., 2016; Gras et al., 2017;  
576 Oelkers et al., 2018), may be reset during mineral phase transformations that occur via  
577 dissolution-reprecipitation, complicating their interpretation.

578

## 579 **5. Conclusions**

580 The hydrated Mg-carbonate minerals nesquehonite and dypingite are common  
581 products of natural and engineered ultramafic rock weathering, and are of interest owing to  
582 their capacity to securely store atmospheric CO<sub>2</sub>. Knowledge of their stability, longevity, and  
583 consequences of transformations will aid in our ability to ascertain the longevity and capacity  
584 of engineered carbon storage operations. In this study, the solubility of nesquehonite was re-  
585 examined, and the solubility of dypingite was measured for the first time. Our nesquehonite  
586 solubility product is in good agreement with the recent modeling study of Wang and Li  
587 (2012), which considered aqueous speciation. Our dypingite solubility product, though  
588 complicated by the presence of multiple dypingite-like phases, nevertheless allows estimation  
589 of dypingite saturation state in natural waters and engineered CO<sub>2</sub> storage operations. A  
590 natural wetland where dypingite has been observed (Power et al., 2007, 2009, 2014) is  
591 demonstrated to be close to equilibrium with respect to dypingite, providing confidence in  
592 our values. Finally, our experimental results indicate that nesquehonite, which tends to form  
593 at greater than atmospheric  $p\text{CO}_2$ , can rapidly transform to dypingite at 25°C and 35°C,  
594 resulting in greater security of CO<sub>2</sub> storage due the higher stability of this phase, but  
595 accompanied by a slight loss of CO<sub>2</sub> to solution. This phase transformation apparently occurs  
596 via a dissolution re-precipitation mechanism, altering external crystal morphology,  
597 potentially releasing trace metals, and likely resetting isotopic signatures.

598

599 **Acknowledgments**

600

601           This research was funded by a Marie Skłodowska-Curie Individual Fellowship  
602 awarded to ALH under grant agreement number 701478 (DryMIN) under the European  
603 Union’s Horizon 2020 program. This study also benefited from the financial support of the  
604 ISIFoR Carnot institute (Institute for the Sustainable Engineering of Fossil Resources) under  
605 the project SERPCARB AAP-2016. Michel Thibaut and Ludovic Menjot are thanked for  
606 their assistance with XRD. We appreciate the assistance of Thierry Aigouy, Stephane Le  
607 Blond du Plouy, and James Davy with SEM, and of Carole Causserand with analyses of  
608 fluids. Andrew Thomson is thanked for access to and assistance with FTIR, which was  
609 supported by the Science and Technology Facilities Council under grant number  
610 ST/K000934/1. Alain Castillo is thanked for his assistance with laboratory apparatus and  
611 Sasha Wilson for valuable advice regarding XRD data. Ian Power generously provided fluid  
612 compositions for the wetland in Atlin, Canada.

613 **References**

614

615 Assima G. P., Larachi F., Beaudoin G. and Molson J. (2012) CO<sub>2</sub> sequestration in chrysotile  
616 mining residues—Implication of watering and passivation under environmental  
617 conditions. *Ind. Eng. Chem. Res.* **51**, 8726–8734.

618 Assima G. P., Larachi F., Molson J. and Beaudoin G. (2014a) Comparative study of five  
619 Québec ultramafic mining residues for use in direct ambient carbon dioxide mineral  
620 sequestration. *Chem. Eng. J.* **245**, 56–64.

621 Assima G. P., Larachi F., Molson J. and Beaudoin G. (2014b) Emulation of ambient carbon  
622 dioxide diffusion and carbonation within nickel mining residues. *Miner. Eng.* **59**, 39–44.

623 Assima G. P., Larachi F., Molson J. and Beaudoin G. (2014c) Impact of temperature and  
624 oxygen availability on the dynamics of ambient CO<sub>2</sub> mineral sequestration by nickel  
625 mining residues. *Chem. Eng. J.* **240**, 394–403.

626 Ballirano P., De Vito C., Ferrini V. and Mignardi S. (2010) The thermal behaviour and  
627 structural stability of nesquehonite, MgCO<sub>3</sub>·3H<sub>2</sub>O, evaluated by in situ laboratory  
628 parallel-beam X-ray powder diffraction: New constraints on CO<sub>2</sub> sequestration within  
629 minerals. *J. Hazard. Mater.* **178**, 522–528.

630 Ballirano P., De Vito C., Mignardi S. and Ferrini V. (2013) Phase transitions in the Mg-CO<sub>2</sub>-  
631 H<sub>2</sub>O system and the thermal decomposition of dypingite, Mg<sub>5</sub>(CO<sub>3</sub>)<sub>4</sub>(OH)<sub>2</sub>·5H<sub>2</sub>O:  
632 Implications for geosequestration of carbon dioxide. *Chem. Geol.* **340**, 59–67.

633 Bea S.A., Wilson S.A., Mayer K. U., Dipple G. M., Power I. M. and Gamazo P. (2012)  
634 Reactive transport modeling of natural carbon sequestration in ultramafic mine tailings.  
635 *Vadose Zone J.* **11**.

636 Beinlich A. and Austrheim H. (2012) In situ sequestration of atmospheric CO<sub>2</sub> at low  
637 temperature and surface cracking of serpentinized peridotite in mine shafts. *Chem. Geol.*

638           **332–333**, 32–44.

639   Beinlich, A., Austrheim, H., Mavromatis, V., Grguric, B., Putnis, C.V., Putnis, A. (2018)

640           Peridotite weathering is the missing ingredient of Earth's continental crust composition.

641           *Nat. Commun.* **9**, 634.

642   Bénézeth P., Berninger U.-N., Bovet N., Schott J. and Oelkers E. H. (2018) Experimental

643           determination of the solubility product of dolomite at 50 to 253°C. *Geochim.*

644           *Cosmochim. Acta* **224**, 262–275.

645   Bénézeth P., Saldi G. D., Dandurand J. L. and Schott J. (2011) Experimental determination of

646           the solubility product of magnesite at 50 to 200°C. *Chem. Geol.* **286**, 21–31.

647   Berninger U.-N., Jordan G., Schott J. and Oelkers E. H. (2014) The experimental

648           determination of hydromagnesite precipitation rates at 22.5 - 75°C. *Mineral. Mag.* **78**,

649           1405–1416.

650   Boschi C., Dini A., Dallai L., Ruggieri G. and Gianelli G. (2009) Enhanced CO<sub>2</sub>-mineral

651           sequestration by cyclic hydraulic fracturing and Si-rich fluid infiltration into

652           serpentinites at Malentrata (Tuscany, Italy). *Chem. Geol.* **265**, 209–226.

653   Canterford J. H., Tsambourakis G. and Lambert B. (1984) Some observations on the

654           properties of dypingite , Mg<sub>5</sub>(CO<sub>3</sub>)<sub>4</sub>(OH)<sub>2</sub>·5H<sub>2</sub>O, and related minerals. *Mineral. Mag.* **48**,

655           437–442.

656   Chaka A. M., Felmy A. R. and Qafoku O. (2016) Ab initio thermodynamics of magnesium

657           carbonates and hydrates in water-saturated supercritical CO<sub>2</sub> and CO<sub>2</sub>-rich regions.

658           *Chem. Geol.* **434**, 1–11.

659   Cheng W. and Li Z. (2010) Nucleation kinetics of nesquehonite (MgCO<sub>3</sub>·3H<sub>2</sub>O) in the

660           MgCl<sub>2</sub>-Na<sub>2</sub>CO<sub>3</sub> system. *J Cryst. Growth.* **312**, 1563–1571.

661   Cheng W. and Li Z. (2009) Precipitation of nesquehonite from homogeneous supersaturated

662           solutions. *Cryst. Res. Technol.* **44**, 937–947.

663 Cheng W., Li Z. and Demopoulos G. P. (2009) Effects of temperature on the preparation of  
664 magnesium carbonate hydrates by reaction of  $\text{MgCl}_2$  with  $\text{Na}_2\text{CO}_3$ . *Chinese J. Chem.*  
665 *Eng.* **17**, 661–666.

666 Davies P. J. and Bubela B. (1973) The transformation of nesquehonite into hydromagnesite.  
667 *Chem. Geol.* **12**, 289–300.

668 Ding W., Ouyang J. and Yang H. (2016) Synthesis and characterization of nesquehonite  
669 ( $\text{MgCO}_3 \cdot 3\text{H}_2\text{O}$ ) powders from natural talc. *Powder Technol.* **292**, 169–175.

670 Dong M., Cheng W., Li Z. and Demopoulos G. P. (2008) Solubility and stability of  
671 nesquehonite ( $\text{MgCO}_3 \cdot \text{H}_2\text{O}$ ) in mixed  $\text{NaCl} + \text{MgCl}_2$ ,  $\text{NH}_4\text{Cl} + \text{MgCl}_2$ ,  $\text{LiCl}$ , and  $\text{LiCl}$   
672  $+ \text{MgCl}_2$  solutions. *J. Chem. Eng. Data* **53**, 2586–2593.

673 Dong M., Li Z., Mi J. and Demopoulos G. P. (2009) Solubility and stability of nesquehonite  
674 ( $\text{MgCO}_3 \cdot 3\text{H}_2\text{O}$ ) in mixed  $\text{NaCl} + \text{MgCl}_2$ ,  $\text{NH}_4\text{Cl} + \text{MgCl}_2$ ,  $\text{LiCl}$ , and  $\text{LiCl} + \text{MgCl}_2$   
675 solutions. *J. Chem. Eng. Data* **54**, 3002–3007.

676 Falk E. S., Guo W., Paukert A. N., Matter J. M., Mervine E. M. and Kelemen P. B. (2016)  
677 Controls on the stable isotope compositions of travertine from hyperalkaline springs in  
678 Oman: Insights from clumped isotope measurements. *Geochim. Cosmochim. Acta* **192**,  
679 1–28.

680 Felmy A. R., Qafoku O., Arey B. W., Hu J. Z., Hu M., Todd Schaefer H., Ilton E. S., Hess N. J.,  
681 Pearce C. I., Feng J. and Rosso K. M. (2012) Reaction of water-saturated supercritical  
682  $\text{CO}_2$  with forsterite: Evidence for magnesite formation at low temperatures. *Geochim.*  
683 *Cosmochim. Acta* **91**, 271–282.

684 Frost R. L., Bahfenne S., Graham J. and Martens W. N. (2008) Thermal stability of artinite,  
685 dypingite and brugnatellite—Implications for the geosequestration of green house gases.  
686 *Thermochim. Acta* **475**, 39–43.

687 Frost R. L. and Palmer S. J. (2011) Infrared and infrared emission spectroscopy of

688 nesquehonite  $\text{Mg}(\text{OH})(\text{HCO}_3) \cdot 2\text{H}_2\text{O}$ -implications for the formula of nesquehonite.  
689 *Spectrochim. Acta - Part A Mol. Biomol. Spectrosc.* **78**, 1255–1260.

690 Garcia del Real P. G., Maher K., Kluge T., Bird D. K., Brown G. E. and John C. M. (2016)  
691 Clumped-isotope thermometry of magnesium carbonates in ultramafic rocks. *Geochim.*  
692 *Cosmochim. Acta.* **193**, 222–250.

693 Gautier Q., Bénézech P., Mavromatis V. and Schott J. (2014) Hydromagnesite solubility  
694 product and growth kinetics in aqueous solution from 25 to 75°C. *Geochim. Cosmochim.*  
695 *Acta* **138**, 1–20.

696 Gerdemann S. J., O'Connor W. K., Dahlin D. C., Penner L. R. and Rush H. (2007) Ex situ  
697 aqueous mineral carbonation. *Environ. Sci. Technol.* **41**, 2587–2593.

698 Gislason S. R. and Oelkers E. H. (2014) Carbon storage in basalt. *Science* **344**, 373–374.

699 Gras A., Beaudoin G., Molson J., Plante B., Bussière B., Lemieux J. M. and Dupont P. P.  
700 (2017) Isotopic evidence of passive mineral carbonation in mine wastes from the  
701 Dumont Nickel Project (Abitibi, Quebec). *Int. J. Greenhouse Gas Control* **60**, 10–23.

702 Hales M., Frost R. and Martens W. (2008) Thermo-raman spectroscopy of synthetic  
703 nesquehonite - implication for the geosequestration of greenhouse gases. *J. Raman*  
704 *Spectrosc.* **38**, 1141–1149.

705 Hamilton J. L., Wilson S. A., Morgan B., Turvey C. C., Paterson D. J., Jowitt S. M.,  
706 McCutcheon J. and Southam G. (2018) Fate of transition metals during passive  
707 carbonation of ultramafic mine tailings via air capture with potential for metal resource  
708 recovery. *Int. J. Greenhouse Gas Control* **71**, 155–167.

709 Hamilton J. L., Wilson S. A., Morgan B., Turvey C. C., Paterson D. J., MacRae C.,  
710 McCutcheon J. and Southam G. (2016) Nesquehonite sequesters transition metals and  
711  $\text{CO}_2$  during accelerated carbon mineralisation. *Int. J. Greenhouse Gas Control.* **55**, 73–  
712 81.

713 Hänchen M., Prigiobbe V., Baciocchi R. and Mazzotti M. (2008) Precipitation in the Mg-  
714 carbonate system—effects of temperature and CO<sub>2</sub> pressure. *Chem. Eng. Sci.* **63**, 1012–  
715 1028.

716 Harrison A. L., Dipple G. M., Power I. M. and Mayer K. U. (2016) The impact of evolving  
717 mineral-water-gas interfacial areas on mineral-fluid reaction rates in unsaturated porous  
718 media. *Chem. Geol.* **421**, 65–80.

719 Harrison A. L., Dipple G. M., Power I. M. and Mayer K. U. (2015) Influence of surface  
720 passivation and water content on mineral reactions in unsaturated porous media:  
721 Implications for brucite carbonation and CO<sub>2</sub> sequestration. *Geochim. Cosmochim. Acta*  
722 **148**, 477–495.

723 Harrison A. L., Dipple G. M., Song W., Power I. M., Mayer K. U., Beinlich A. and Sinton D.  
724 (2017) Changes in mineral reactivity driven by pore fluid mobility in partially wetted  
725 porous media. *Chem. Geol.* **463**, 1–11.

726 Harrison A. L., Power I. M. and Dipple G. M. (2013a) Accelerated carbonation of brucite in  
727 mine tailings for carbon sequestration. *Environ. Sci. Technol.* **47**, 126–134.

728 Harrison A. L., Power I. M. and Dipple G. M. (2013b) Strategies for enhancing carbon  
729 sequestration in Mg-rich mine tailings. In *Reliable Mine Water Technology (Vol. 1)* (eds.  
730 A. Brown, L. Figueroa, and C. Wolkersdorfer). Publication Printers, Denver, Colorado,  
731 USA. pp. 593–598.

732 Hartmann J., West J., Renforth P., Kohler P., De La Rocha C., Wolf-Gladrow D. A., Durr H.  
733 and Scheffran J. (2013) Enhanced chemical weathering as a geoengineering strategy to  
734 reduce atmospheric carbon dioxide, a nutrient source and to mitigate ocean acidification.  
735 *Rev. Geophys.* **51**, 113–149.

736 Helgeson H. C. (1969) Thermodynamics of hydrothermal systems at elevated temperatures  
737 and pressures. *Am. J. Sci.* **267**, 729–804.

738 Highfield J., Chen J., Haghughatlari M., Abacka J. and Zevenhoven R. (2016) Low-  
739 temperature gas-solid carbonation of magnesia and magnesium hydroxide promoted by  
740 non-immersive contact with water. *R. Soc. Chem. Adv.* **6**, 89655–89664.

741 Hopkinson L., Kristova P., Rutt K. and Cressey G. (2012) Phase transitions in the system  
742 MgO – CO<sub>2</sub> – H<sub>2</sub>O during CO<sub>2</sub> degassing of Mg-bearing solutions. *Geochim.*  
743 *Cosmochim. Acta* **76**, 1–13.

744 Hopkinson L., Rutt K. and Cressey G. (2008) The transformation of nesquehonite to  
745 hydromagnesite in the system CaO-MgO-H<sub>2</sub>O-CO<sub>2</sub>: An experimental spectroscopic  
746 study. *J. Geol.* **116**, 387–400.

747 Hostetler P. (1964) The degree of saturation of magnesium and calcium carbonate minerals in  
748 natural waters. *Int. Assoc. Sci. Hydrol.* **64**, 34–49.

749 Hövelmann J., Putnis C. V, Ruiz-Agudo E. and Austrheim H. (2012) Direct nanoscale  
750 observations of CO<sub>2</sub> sequestration during brucite [Mg(OH)<sub>2</sub>] dissolution. *Environ. Sci.*  
751 *Technol.* **46**, 5253–5260.

752 Jauffret G., Morrison J. and Glasser F. P. (2015) On the thermal decomposition of  
753 nesquehonite. *J. Therm. Anal. Calorim.*, 5–10.

754 Kazakov A. V., Tikhomirova M. M. and Plotnikova V. I. (1959) The system of carbonate  
755 equilibria. *Int. Geol. Rev.* **1**, 1–39.

756 Kelemen P. B. and Matter J. (2008) In situ carbonation of peridotite for CO<sub>2</sub> storage. *Proc.*  
757 *Natl. Acad. Sci.* **105**, 17295–17300.

758 Kline W. (1929) The solubility of magnesium carbonate (nesquehonite) in water at 25° and  
759 pressures of carbon dioxide up to one atmosphere. *J. Am. Chem. Soc.* **51**, 2093–2097.

760 Königsberger E., Königsberger L.-C. and Gamsjäger H. (1999) Low-temperature  
761 thermodynamic model for the system Na<sub>2</sub>CO<sub>3</sub>-MgCO<sub>3</sub>-CaCO<sub>3</sub>-H<sub>2</sub>O. *Geochim.*  
762 *Cosmochim. Acta* **63**, 3105–3119.



763 Kristova P., Hopkinson L. J., Rutt K. J., Hunter H. M. A. and Cressey G. (2014) Carbonate  
764 mineral paragenesis and reaction kinetics in the system MgO–CaO–CO<sub>2</sub>–H<sub>2</sub>O in  
765 presence of chloride or nitrate ions at near surface ambient temperatures. *Appl.*  
766 *Geochemistry* **50**, 16–24.

767 Lackner K. S. (2003) A Guide to CO<sub>2</sub> Sequestration. *Science* **300**, 1677–1678.

768 Lackner K. S., Wendt C. H., Butt D. P., Joyce E. L. and Sharp D. H. (1995) Carbon dioxide  
769 disposal in carbonate minerals. *Energy* **20**, 1153–1170.

770 Lanas J. and Alvarez J. I. (2004) Dolomitic lime: Thermal decomposition of nesquehonite.  
771 *Thermochim. Acta* **421**, 123–132.

772 Langmuir D. (1965) Stability of carbonates in the system MgO–CO<sub>2</sub>–H<sub>2</sub>O. *J. Geol.* **73**, 730–  
773 754.

774 Lin Y., Zheng M. and Ye C. (2017) Hydromagnesite precipitation in the alkaline lake Dujiali,  
775 central Qinghai-Tibetan Plateau: Constraints on hydromagnesite precipitation from  
776 hydrochemistry and stable isotopes. *Appl. Geochem.* **78**, 139–148.

777 Loring J. S., Thompson C. J., Zhang C., Wang Z., Schaef H. T. and Rosso K. M. (2012) In  
778 situ infrared spectroscopic study of brucite carbonation in dry to water-saturated  
779 supercritical carbon dioxide. *J. Phys. Chem. A* **116**, 4768–4777.

780 Marion G. (2001) Carbonate mineral solubility at low temperatures in the Na–K–Mg–Ca–H–  
781 Cl–SO<sub>4</sub>–OH–HCO<sub>3</sub>–CO<sub>3</sub>–CO<sub>2</sub>–H<sub>2</sub>O system. *Geochim. Cosmochim. Acta* **65**, 1883–1896.

782 Matter J., Stute M., Snæbjörnsdóttir S. Ó., Oelkers E., Gislason S. R., Aradóttir E. S.,  
783 Sigfusson B., Gunnarsson I., Alfredsson H. A., Wolff-boenisch D., Mesfin K.,  
784 Fernandez de la Reguera Taya D., Hall J., Dideriksen K. and Broecker W. S. (2016)  
785 Rapid carbon mineralization for permanent disposal of anthropogenic carbon dioxide  
786 emissions. *Science* **352**, 1312–1314.

787 Mavromatis, V., Bundeleva, I.A., Shirokova, L.S., Millo, C., Pokrovsky, O.S., Bénézech, P.,

788 Ader, M., Oelkers, E.H. (2015) The continuous re-equilibration of carbon isotope  
789 compositions of hydrous Mg carbonates in the presence of cyanobacteria. *Chem. Geol.*  
790 **404**, 41-51.

791 Mavromatis V., Pearce C. R., Shirokova L. S., Bundeleva I. A., Pokrovsky O. S., Bénézeth P.  
792 and Oelkers E. H. (2012) Magnesium isotope fractionation during hydrous magnesium  
793 carbonate precipitation with and without cyanobacteria. *Geochim. Cosmochim. Acta* **76**,  
794 161–174.

795 McClain C. N. and Maher K. (2016) Chromium fluxes and speciation in ultramafic  
796 catchments and global rivers. *Chem. Geol.* **426**, 135–157.

797 McCutcheon J., Power I. M., Harrison A. L., Dipple G. M. and Southam G. (2014) A  
798 greenhouse-scale photosynthetic microbial bioreactor for carbon sequestration in  
799 magnesium carbonate minerals. *Environ. Sci. Technol.* **48**, 9142–9151.

800 McCutcheon J., Turvey C. C., Wilson S.A., Hamilton J. L. and Southam G. (2017)  
801 Experimental deployment of microbial mineral carbonation at an asbestos mine:  
802 Potential applications to carbon storage and tailings stabilization. *Minerals* **7**, 15–18.

803 McCutcheon J., Wilson S. A. and Southam G. (2016) Microbially accelerated carbonate  
804 mineral precipitation as a strategy for in situ carbon sequestration and rehabilitation of  
805 asbestos mine sites. *Environ. Sci. Technol.*, **50**, 1419–1423.

806 Mervine E. M., Humphris S. E., Sims K. W. W., Kelemen P. B. and Jenkins W. J. (2014)  
807 Carbonation rates of peridotite in the Samail Ophiolite, Sultanate of Oman, constrained  
808 through <sup>14</sup>C dating and stable isotopes. *Geochim. Cosmochim. Acta* **126**, 371–397.

809 Montes-Hernandez G., Renard F., Chiriack R., Findling N. and Toche F. (2012) Rapid  
810 precipitation of magnesite microcrystals from Mg(OH)<sub>2</sub> - H<sub>2</sub>O - CO<sub>2</sub> slurry enhanced by  
811 NaOH and a heat-aging step (from ~20 to 90 °C). *Cryst. Growth Des.* **12**, 5233–5240.

812 Montserrat F., Renforth P., Hartmann J., Knops P., Leermakers M. and Meysman F. J. R.

813 (2017) Olivine dissolution in seawater: Implications for CO<sub>2</sub> sequestration through  
814 Enhanced Weathering in coastal environments. *Environ. Sci. Technol.* **51**, 3960–3972.

815 Morgan B., Wilson S. A., Madsen I. C., Gozukara Y. M. and Habsuda J. (2015) Increased  
816 thermal stability of nesquehonite (MgCO<sub>3</sub>·3H<sub>2</sub>O) in the presence of humidity and CO<sub>2</sub>:  
817 Implications for low-temperature CO<sub>2</sub> storage. *Int. J. Greenhouse Gas Control* **39**, 366–  
818 376.

819 Oelkers, E.H., Berninger, U.N., Perez-Fernandez, A., Chmeleff, J., Mavromatis, V. (2018)  
820 The temporal evolution of magnesium isotope fractionation during hydromagnesite  
821 dissolution, precipitation, and at equilibrium. *Geochim. Cosmochim. Acta* **226**, 36-49.

822 Oelkers E. H. and Cole D. R. (2008) Carbon dioxide sequestration: A solution to a global  
823 problem. *Elements* **4**, 305–310.

824 Oskierski H. C., Dlugogorski B. Z. and Jacobsen G. (2013) Sequestration of atmospheric CO<sub>2</sub>  
825 in chrysotile mine tailings of the Woodsreef Asbestos Mine, Australia: Quantitative  
826 mineralogy, isotopic fingerprinting and carbonation rates. *Chem. Geol.* **358**, 156–169.

827 Oskierski H. C., Dlugogorski B. Z., Oliver T. K. and Jacobsen G. (2016) Chemical and  
828 isotopic signatures of waters associated with the carbonation of ultramafic mine tailings,  
829 Woodsreef Asbestos Mine, Australia. *Chem. Geol.* **436**, 11–23.

830 Palmer D. A. and Wesolowski D. J. (1997) Potentiometric measurements of the first  
831 hydrolysis quotient of magnesium (II) to 250°C and 5 molal ionic strength ( NaCl ). *J.*  
832 *Solution Chem.* **26**, 2167–232.

833 Parkhurst D. L. and Appelo C. A. J. (2013) Description of Input and Examples for  
834 PHREEQC Version 3 — A Computer Program for Speciation , Batch-Reaction , One-  
835 Dimensional Transport , and Inverse Geochemical Calculations. In *U.S. Geological*  
836 *Survey Techniques and Methods, book 6, chap. A43, 497 p.* Denver, Colorado. p. 497.

837 Patterson C. S., Busey R. H. and Mesmer R. E. (1984) Second ionization of carbonic acid in

838 NaCl media to 250°C. *J. Solution Chem.* **13**, 647–661.

839 Patterson C. S., Slocum G. H., Busey R. H. and Mesmer R. E. (1982) Carbonate equilibria in  
840 hydrothermal systems: First ionization of carbonic acid in NaCl media to 300°C.  
841 *Geochim. Cosmochim. Acta* **46**, 1653–1663.

842 Power I. M., Dipple G. M. and Southam G. (2010) Bioleaching of ultramafic tailings by  
843 *Acidithiobacillus* spp. for CO<sub>2</sub> sequestration. *Environ. Sci. Technol.* **44**, 456–462.

844 Power I. M., Harrison A. L. and Dipple G. M. (2016) Accelerating mineral carbonation using  
845 carbonic anhydrase. *Environ. Sci. Technol.* **50**, 2610–2618.

846 Power I. M., Harrison A. L., Dipple G. M. and Southam G. (2013c) Carbon sequestration via  
847 carbonic anhydrase facilitated magnesium carbonate precipitation. *Int. J. Greenhouse*  
848 *Gas Control* **16**, 145–155.

849 Power I. M., Harrison A. L., Dipple G. M., Wilson S. A., Kelemen P. B., Hitch M. and  
850 Southam G. (2013a) Carbon mineralization: From natural analogues to engineered  
851 systems. *Rev. Mineral. Geochemistry* **77**, 305–360.

852 Power I. M., Kenward P. A., Dipple G. M. and Raudsepp M. (2017) Room temperature  
853 magnesite precipitation. *Cryst. Growth Des.* **17**, 5652–5659.

854 Power I. M., McCutcheon J., Harrison A. L., Wilson S. A., Dipple G. M., Kelly S., Southam  
855 C. and Southam G. (2014a) Strategizing carbon-neutral mines: A Case for pilot projects.  
856 *Minerals* **4**, 399–436.

857 Power I. M., Wilson S. A. and Dipple G. M. (2013b) Serpentinite carbonation for CO<sub>2</sub>  
858 sequestration. *Elements* **9**, 115–121.

859 Power I. M., Wilson S. A., Harrison A. L., Dipple G. M., McCutcheon J., Southam G. and  
860 Kenward P. A. (2014b) A depositional model for hydromagnesite-magnesite playas near  
861 Atlin, British Columbia, Canada. *Sedimentology* **61**, 1701–1733.

862 Power I. M., Wilson S. A., Thom J. M., Dipple G. M., Gabites J. E. and Southam G. (2009)

863 The hydromagnesite playas of Atlin, British Columbia, Canada: A biogeochemical  
864 model for CO<sub>2</sub> sequestration. *Chem. Geol.* **260**, 286–300.

865 Power I. M., Wilson S. A., Thom J. M., Dipple G. M. and Southam G. (2007) Biologically  
866 induced mineralization of dypingite by cyanobacteria from an alkaline wetland near  
867 Atlin, British Columbia, Canada. *Geochem. Trans.* **8**, 13.

868 Pronost J., Beaudoin G., Lemieux J.-M., Hebert R., Constantin M., Marcouiller S., Klein M.,  
869 Duchesne J., Molson J. W., Larachi F. and Maldague X. (2012) CO<sub>2</sub>-depleted warm air  
870 venting from chrysotile milling waste (Thetford Mines, Canada): Evidence for in-situ  
871 carbon capture from the atmosphere. *Geology* **40**, 275–278.

872 Pronost J., Beaudoin G., Tremblay J., Larachi F., Duchesne J., Hébert R. and Constantin M.  
873 (2011) Carbon sequestration kinetic and storage capacity of ultramafic mining waste.  
874 *Environ. Sci. Technol.* **45**, 9413–9420.

875 Raade G. (1970) Dypingite, a new hydrous basic carbonate of magnesium, from Norway. *Am.*  
876 *Mineral.* **55**, 1457–1465.

877 Renforth P. (2012) The potential of enhanced weathering in the UK. *Int. J. Greenhouse Gas*  
878 *Control* **10**, 229–243.

879 Rigopoulos I., Harrison A. L., Delimitis A., Ioannou I., Efstathiou A. M., Kyratsi T. and  
880 Oelkers E. H. (2018) Carbon sequestration via enhanced weathering of peridotites and  
881 basalts in seawater. *Appl. Geochem.* **91**, 197–207.

882 Robie R. A. and Hemingway B. S. (1972) The heat capacities at low-temperatures and  
883 entropies at 298.15 K of nesquehonite, MgCO<sub>3</sub>·3H<sub>2</sub>O, and hydromagnesite. *Am. Mineral.*  
884 **57**, 1768–1781.

885 Robie R. and Hemingway B. (1973) The enthalpies of formation of nesquehonite,  
886 MgCO<sub>3</sub>·3H<sub>2</sub>O, and hydromagnesite, 5MgO·4CO<sub>2</sub>·5H<sub>2</sub>O. *J. Res. U.S. Geol. Surv.* **1**,  
887 543–547.

888 Ruiz-Agudo E., Putnis C. V., Rodriguez-Navarro C. and Putnis A. (2012) Mechanism of  
889 leached layer formation during chemical weathering of silicate minerals. *Geology* **40**,  
890 947–950.

891 Saldi G. D., Jordan G., Schott J. and Oelkers E. H. (2009) Magnesite growth rates as a  
892 function of temperature and saturation state. *Geochim. Cosmochim. Acta* **73**, 5646–5657.

893 Saldi G. D., Schott J., Pokrovsky O. S., Gautier Q. and Oelkers E. H. (2012) An experimental  
894 study of magnesite precipitation rates at neutral to alkaline conditions and 100–200°C as  
895 a function of pH, aqueous solution composition and chemical affinity. *Geochim.*  
896 *Cosmochim. Acta* **83**, 93–109.

897 Schaef H. T., Mcgrail B. P., Loring J. L., Bowden M. E., Arey B. W. and Rosso K. M. (2013)  
898 Forsterite [Mg<sub>2</sub>SiO<sub>4</sub>] carbonation in wet supercritical CO<sub>2</sub>: An in situ high-pressure X-  
899 ray diffraction study. *Environ. Sci. Technol.* **47**, 174–181.

900 Schaef H. T., Windisch C. F., McGrail B. P., Martin P. F. and Rosso K. M. (2011) Brucite  
901 [Mg(OH)<sub>2</sub>] carbonation in wet supercritical CO<sub>2</sub>: An in situ high pressure X-ray  
902 diffraction study. *Geochim. Cosmochim. Acta* **75**, 7458–7471.

903 Schuiling R. D. and Boer P. L. De (2010) Coastal spreading of olivine to control atmospheric  
904 CO<sub>2</sub> concentrations: A critical analysis of viability. Comment: Nature and laboratory  
905 models are different. *Int. J. Greenhouse Gas Control* **4**, 855–856.

906 Shirokova L. S., Mavromatis V., Bundeleva I. A., Pokrovsky O. S., Bénézech P., Gérard E.,  
907 Pearce C. R. and Oelkers E. H. (2013) Using Mg isotopes to trace cyanobacterially  
908 mediated magnesium carbonate precipitation in alkaline lakes. *Aquat. Geochemistry* **19**,  
909 1–24.

910 Shock E. L. and Helgeson H. C. (1988) Calculation of the thermodynamic and transport  
911 properties of aqueous species at high pressures and temperatures: Correlation algorithms  
912 for ionic species and equation of state predictions to 5 kb and 1000°C. *Geochim.*

913 *Cosmochim. Acta* **52**, 2009–2036.

914 Shock E. L., Sassani D. C., Willis M. and Sverjensky D. A. (1997) Inorganic species in  
915 geologic fluids: Correlations among standard molal thermodynamic properties of  
916 aqueous ions and hydroxide complexes. *Geochim. Cosmochim. Acta* **61**, 907–950.

917 Stefansson A., Bénézech P., and Schott J. (2014) Potentiometric and spectrophotometric  
918 study of the stability of magnesium carbonate and bicarbonate pairs to 150C and  
919 aqueous inorganic carbon speciation and magnesite solubility. *Geochim. Cosmochim.*  
920 *Acta* **138**, 21–31.

921 Sundquist E. T. (1993) The global carbon dioxide budget. *Science*. **259**, 934–941.

922 Sutradhar N., Sinhamahapatra A., Pahari S. K., Pal P., Bajaj H. C., Mukhopadhyay I. and  
923 Panda A. B. (2011) Controlled synthesis of different morphologies of MgO and their use  
924 as solid base catalysts. *J. Phys. Chem. C* **115**, 12308–12316.

925 Vágvölgyi V., Hales M., Frost R. L., Locke A., Kristóf J. and Horváth E. (2008)  
926 Conventional and controlled rate thermal analysis of nesquehonite  $Mg(HCO_3)(OH) \cdot 2$   
927  $(H_2O)$ . *J. Therm. Anal. Calorim.* **94**, 523–528.

928 Wagman D. D., Evans W. H., Parker V. B., Schumm R. H., Halow I., Bailey S. M., Churney  
929 K. L. and Nuttall R. L. (1982) The NBS tables of chemical thermodynamic properties:  
930 selected values for inorganic and C1 and C2 organic substances in SI units. *J. Chem. Ref.*  
931 *Data*, 392, 11(supplement n. 2).

932 Wang D. and Li Z. (2012) Chemical modeling of nesquehonite solubility in Li + Na + K +  
933  $NH_4$  + Mg + Cl +  $H_2O$  System with a speciation-based approach. *Chinese J. Chem. Eng.*  
934 **20**, 2670276.

935 Wang Y., Li Z. and Demopoulos G. P. (2008) Controlled precipitation of nesquehonite  
936  $(MgCO_3 \cdot 3H_2O)$  by the reaction of  $MgCl_2$  with  $(NH_4)_2CO_3$ . **310**, 1220–1227.

937 Wilson S. A., Barker S. L. L., Dipple G. M. and Atudorei V. (2010) Isotopic disequilibrium

938 during uptake of atmospheric CO<sub>2</sub> into mine process waters: Implications for CO<sub>2</sub>  
939 sequestration. *Environ. Sci. Technol.* **44**, 9522–9529.

940 Wilson S. A., Dipple G. M., Power I. M., Barker S. L. L., Fallon S. J. and Southam G. (2011)  
941 Subarctic weathering of mineral wastes provides a sink for atmospheric CO<sub>2</sub>. *Environ.*  
942 *Sci. Technol.* **45**, 7727–7736.

943 Wilson S. A., Dipple G. M., Power I. M., Thom J. M., Anderson R. G., Raudsepp M.,  
944 Gabites J. E. and Southam G. (2009) Carbon dioxide fixation within mine wastes of  
945 ultramafic-hosted ore deposits: Examples from the Clinton Creek and Cassiar chrysotile  
946 deposits, Canada. *Econ. Geol.* **104**, 95–112.

947 Wilson S. A., Harrison A. L., Dipple G. M., Power I. M., Barker S. L. L., Mayer K. U.,  
948 Fallon S. J., Raudsepp M. and Southam G. (2014) Offsetting of CO<sub>2</sub> emissions by air  
949 capture in mine tailings at the Mount Keith Nickel Mine, Western Australia: Rates,  
950 controls and prospects for carbon neutral mining. *Int. J. Greenhouse Gas Control* **25**,  
951 121–140.

952 Wilson S. A., Raudsepp M. and Dipple G. M. (2009) Quantifying carbon fixation in trace  
953 minerals from processed kimberlite: A comparative study of quantitative methods using  
954 X-ray powder diffraction data with applications to the Diavik Diamond Mine, Northwest  
955 Territories, Canada. *Appl. Geochem.* **24**, 2312–2331.

956 Wilson S. A., Raudsepp M. and Dipple G. M. (2006) Verifying and quantifying carbon  
957 fixation in minerals from serpentine-rich mine tailings using the Rietveld method with  
958 X-ray powder diffraction data. *Am. Mineral.* **91**, 1331–1341.

959 Xiong Y. (2011) Experimental determination of solubility constant of hydromagnesite (5424)  
960 in NaCl solutions up to 4.4 m at room temperature. *Chem. Geol.* **284**, 262–269.

961 Xiong Y. and Lord A. S. (2008) Experimental investigations of the reaction path in the  
962 MgO–CO<sub>2</sub>–H<sub>2</sub>O system in solutions with various ionic strengths, and their applications



963 to nuclear waste isolation. *Appl. Geochem.* **23**, 1634–1659.

964 Zhang Z., Zheng Y., Ni Y., Liu Z., Chen J. and Liang X. (2006) Temperature- and pH-  
965 dependent morphology and FT-IR analysis of magnesium carbonate hydrates. *J. Phys.*  
966 *Chem. B* **110**, 12969–12973.

967 Zhao L., Sang L., Chen J., Ji J. and Teng H. H. (2010) Aqueous carbonation of natural  
968 brucite: Relevance to CO<sub>2</sub> sequestration. *Environ. Sci. Technol.* **44**, 406–411.

969 Zhao L., Zhu C., Ji J., Chen J. and Teng H. H. (2013) Thermodynamic and kinetic effect of  
970 organic solvent on the nucleation of nesquehonite. **106**, 192–202.

971

972 **Tables**

973 Table 1. Aqueous composition, aqueous activities, and mineralogical composition measured

974 over time for all experiments.

Experiment	Time (h) <sup>a</sup>	pH (±0.03)	Alkalinity (× 10 <sup>-2</sup> mol/L; ±0.36 × 10 <sup>-2</sup> )	DIC <sup>b</sup> (× 10 <sup>-2</sup> mol/L; ±0.36 × 10 <sup>-2</sup> )	Mg (× 10 <sup>-2</sup> mol/L)	Mg error (3σ × 10 <sup>-2</sup> )	a <sub>Mg2+</sub> <sup>c</sup> (× 10 <sup>-3</sup> )	a <sub>CO3<sup>2-</sup></sub> <sup>c</sup> (× 10 <sup>-3</sup> )	a <sub>H2O</sub> <sup>c</sup>	Mineralogy <sup>d</sup>
5	0	8.25	5.95	6.00				0.19	0.995	nsq
	6	9.44	9.04	7.54	1.214	0.005	2.431	2.88	0.994	nsq
	9	9.40	8.90	7.54	1.157	0.004	2.381	2.65	0.994	nsq
	12	9.41	8.94	7.49	1.290	0.012	2.641	2.71	0.994	nsq
	24	9.39	9.17	7.75	1.269	0.010	2.586	2.70	0.994	nsq
	49	9.43	9.16	7.65	1.278	0.017	2.558	2.87	0.994	nsq
	120 (nsq)	9.47	9.66	7.91	1.510	0.006	2.915	3.15	0.994	nsq
	367 (nsq)	9.59	9.71	7.66	1.505	0.006	2.734	3.76	0.994	nsq
	1085 (nsq)	9.39	9.68	8.14	1.498	0.016	3.001	2.78	0.994	nsq
	1420 (nsq)	9.59	9.67	7.62	1.502	0.014	2.732	3.75	0.994	nsq
25_short	0	8.15	5.94	5.97				0.25	0.995	nsq
	4	9.20	8.99	7.52	1.167	0.015	1.976	2.85	0.994	nsq
	6	9.20	8.99	7.55	1.094	0.011	1.847	2.86	0.994	nsq
	8	9.19	8.87	7.47	1.119	0.003	1.926	2.75	0.994	nsq
	10	9.18	8.61	7.27	1.075	0.019	1.882	2.67	0.994	nsq
	12	9.20	8.72	7.31	1.114	0.008	1.920	2.76	0.994	nsq
	24 (nsq)	9.19	8.95	7.50	1.197	0.013	2.048	2.79	0.994	nsq
	49 (nsq)	9.19	8.97	7.52	1.183	0.002	2.022	2.79	0.994	nsq
	120 (nsq)	9.20	9.02	7.54	1.192	0.011	2.019	2.85	0.994	nsq
	367 (nsq)	9.19	9.05	7.59	1.216	0.015	2.076	2.79	0.994	nsq
	1086	8.97	8.99	8.00	1.113	0.006	2.158	1.95	0.994	nsq+dyp
25_long	0	8.23	5.92	5.92	0.006	0.001	0.002	0.30	0.995	nsq
	22 (nsq)	9.27	8.68	7.12	1.105	0.011	1.821	3.08	0.994	nsq (minor dyp)
	122 (nsq)	9.23	8.69	7.23	1.098	0.009	1.861	2.88	0.994	nsq
	359	8.94	8.69	7.77	1.119	0.012	2.249	1.78	0.994	nsq+dyp
	599	8.82	8.66	7.95	1.075	0.001	2.296	1.42	0.994	nsq+dyp
	843	8.88	8.69	7.87	1.104	0.007	2.288	1.59	0.994	nsq+dyp
	987	8.86	8.09	7.38	1.011	0.020	2.187	1.43	0.994	nsq+dyp
	1157	8.82	8.49	7.80	1.065	0.012	2.303	1.38	0.994	dyp+nsq
	1367 (dyp)	8.81	8.49	7.81	1.069	0.010	2.325	1.35	0.994	dyp+dyp-like
	1607 (dyp)	8.81	8.61	7.93	1.051	0.062	2.265	1.38	0.994	dyp+dyp-like
	2043 (dyp)	8.90	8.49	7.68	1.036	0.008	2.148	1.62	0.994	dyp+dyp-like

975

976

977 Table 1 (continued). Aqueous composition, aqueous activities, and mineralogical  
 978 composition measured over time for all experiments.

Experiment	Time (h) <sup>a</sup>	pH (±0.03)	Alkalinity (× 10 <sup>-2</sup> mol/L; ±0.36 × 10 <sup>-2</sup> )	DIC <sup>b</sup> (× 10 <sup>-2</sup> mol/L; ±0.36 × 10 <sup>-2</sup> )	Mg (× 10 <sup>-2</sup> mol/L)	Mg error (3σ × 10 <sup>-2</sup> )	a <sub>Mg2+</sub> <sup>c</sup> (× 10 <sup>-3</sup> )	a <sub>CO32-</sub> <sup>c</sup> (× 10 <sup>-3</sup> )	a <sub>H2O</sub> <sup>c</sup>	Mineralogy <sup>d</sup>
35_short	0	8.11	5.94	5.96	0.004	nd <sup>e</sup>	0.001	0.28	0.995	nsq
	3 (nsq)	9.12	8.77	7.35	1.051	0.008	1.629	2.82	0.994	nsq
	5 (nsq)	9.12	8.64	7.24	1.063	0.018	1.670	2.75	0.994	nsq
	7 (nsq)	9.14	8.63	7.21	1.047	0.015	1.625	2.83	0.994	nsq
	11 (nsq)	9.11	8.65	7.27	1.050	0.016	1.654	2.73	0.994	nsq
	24 (nsq)	9.22	8.74	7.11	1.048	0.010	1.519	3.26	0.994	nsq
	75	9.19	8.75	7.18	1.062	0.004	1.573	3.12	0.994	nsq (trace dyp)
	122	9.12	8.74	7.33	1.054	0.007	1.647	2.78	0.994	nsq+dyp
	191	9.04	8.78	7.52	1.080	0.008	1.778	2.45	0.994	nsq+dyp
	243	9.02	8.65	7.46	1.048	0.011	1.767	2.32	0.994	nsq+dyp
432	8.84	8.43	7.61	0.900	0.004	1.705	1.70	0.994	dyp+nsq	
35_long	0	8.08	5.93	5.96	0.001	0.0001	0.004	0.26	0.995	nsq
	26 (nsq)	9.17	8.54	7.06	1.044	0.002	1.596	2.95	0.994	nsq
	74 (nsq)	9.20	8.57	7.02	1.056	0.009	1.577	3.10	0.994	nsq
	123	9.09	8.60	7.26	1.057	0.015	1.697	2.64	0.994	nsq (trace dyp)
	244	8.90	8.66	7.66	1.138	0.011	2.082	1.89	0.994	nsq+dyp
	311	8.80	8.14	7.37	1.048	0.002	2.087	1.50	0.994	dyp+nsq
	482 (dyp)	8.65	8.36	7.80	0.951	0.007	2.018	1.16	0.994	dyp
	552 (dyp)	8.64	7.58	7.09	0.922	0.009	2.057	1.03	0.994	dyp
	600 (dyp)	8.63	8.29	7.77	0.930	0.007	1.999	1.10	0.994	dyp
	718	8.63	8.18	7.67	0.915	0.007	1.977	1.10	0.994	dyp+ unknown phase

979 <sup>a</sup>(nsq) indicates time points used for the calculation of  $K_{sp}^{nsq}$ , and (dyp) indicates timepoints used for the calculation of  $K_{sp}^{dyp}$

980 <sup>b</sup>DIC = dissolved inorganic carbon; calculated using PHREEQC V3

981 <sup>c</sup>Aqueous activity calculated using PHREEQC V3

982 <sup>d</sup>determined with X-ray diffraction

983 <sup>e</sup>No data

984

985

986

987

988

989

990 Table 2. Solubility products for nesquehonite and dypingite from this study and previous  
 991 works including the PHREEQC databases.

Temperature (°C)	<i>Nesquehonite log K<sub>sp</sub><sup>nsq</sup></i>							<i>Dypingite log K<sub>sp</sub><sup>dyp</sup></i>		
	<i>this study</i> ±3σ	PHREEQC		<i>Wang and Li</i> (2012)	<i>Kline</i> (1929)	<i>Langmuir</i> (1965)	<i>Hostetler</i> (1964)	<i>this study</i>		
		<i>Minteqv4</i>	<i>LLNL</i>					<i>a<sub>H2O=1</sub></i> ±3σ	<i>a<sub>SH2O</sub></i> ±3σ	<i>a<sub>5H2O</sub></i> ±3σ
5	-5.03±0.13	-4.36	-4.53	-4.99						
25	-5.27±0.15	-4.67	-5.06	-5.27	-4.96	-5.59±0.1 -5.42*	-5.51	-34.93±0.58	-34.95±0.58	-34.94±0.58
35	-5.34±0.04	-4.81	-5.23	-5.40				-36.02±0.31	-36.04±0.31	-36.03±0.31

992 \* considering the MgHCO<sub>3</sub><sup>+</sup> and/or MgCO<sub>3</sub><sup>o</sup> aqueous complexes (reported by Robie and  
 993 Hemingway (1973) based on the data of Langmuir (1965)).

994

995

996 Table 3. Standard state properties (25°C, 1 bar) of nesquehonite reported in the literature and  
 997 determined in this study, and standard state properties of dypingite determined in this study.  
 998 The standard state properties of aqueous species used to calculate the Gibbs free energy of  
 999 formation of nesquehonite and dypingite in the present study are reported in the lower table,  
 1000 as are the equilibrium constants of the considered aqueous Mg complexes at 25°C.

<i>Nesquehonite [MgCO<sub>3</sub>·3H<sub>2</sub>O]</i>				
Source	$\Delta G_r^\circ$ (kJ/mol)	$\Delta G_f^\circ$ (kJ/mol)	$\Delta H_r^\circ$ (kJ/mol)	$\Delta H_f^\circ$ (kJ/mol)
this study	30.1±0.8	-1723.5±0.8	-17.17	-1981.5
Robie and Hemingway (1973)		-1723.8±0.5		-1977.3±0.5
Langmuir (1965)		-1726.6±2.1		
<i>Dypingite [Mg<sub>5</sub>(CO<sub>3</sub>)<sub>4</sub>(OH)<sub>2</sub>·8H<sub>2</sub>O]</i>				
this study	199.4±1.3	-6792.7±1.3		
<i>Aqueous Species</i>				
Source	Species	$\Delta G_f^\circ$ (kJ/mol)	S (J/mol/K)	$\Delta H_f^\circ$ (kJ/mol)
Wagman et al (1982)	H <sub>2</sub> O	-237.13	69.95	-285.83
Shock and Helgeson (1988), Shock et al (1997)	Mg <sup>2+</sup>	-453.98	-138.07	-465.96
Shock and Helgeson (1988)	CO <sub>3</sub> <sup>2-</sup>	-527.98	-50.00	-675.24
Wagman et al (1982)	HCO <sub>3</sub> <sup>-</sup>	-586.77	91.20	-691.99
Wagman et al (1982)	OH <sup>-</sup>	-157.24	-10.75	-229.99
<i>Aqueous Complexes</i>				
Source	Species	<i>log K</i>	Reaction	
Stefansson et al (2014)	MgHCO <sub>3</sub> <sup>+</sup>	1.1	Mg <sup>2+</sup> + HCO <sub>3</sub> <sup>-</sup> ⇌ MgHCO <sub>3</sub> <sup>+</sup>	
Stefansson et al (2014)	MgCO <sub>3</sub> <sup>°</sup>	3.0	Mg <sup>2+</sup> + CO <sub>3</sub> <sup>2-</sup> ⇌ MgCO <sub>3</sub> <sup>°</sup>	
Palmer and Wesolowski (1997)	Mg(OH) <sup>+</sup>	-11.7	Mg <sup>2+</sup> + H <sub>2</sub> O ⇌ MgOH <sup>+</sup> + H <sup>+</sup>	
PHREEQC V3 LLNL database	MgCl <sup>+</sup>	-0.1	Mg <sup>2+</sup> + Cl <sup>-</sup> ⇌ MgCl <sup>+</sup>	

1001

1002

1003 Table 4. Calculated saturation indices for nesquehonite and dypingite from an experimental  
 1004 study (Mavromatis et al., 2012) and a natural Mg-rich wetland (Power et al., 2014).

<b>Mg-carbonate precipitation experiments (data from Mavromatis et al. 2012)</b>				
<b>Experiment</b>	<b>Experiment type</b>	<b>Precipitated mineral</b>	<b>Saturation index</b>	
			<b>nesquehonite</b>	<b>dypingite</b>
Abio-A-1	Abiotic	Nesquehonite	-0.52	-2.10
Abio-A-5	Abiotic	Dypingite	0.06	2.19
Abio-A-10	Abiotic	Dypingite	-0.05	1.67
Abio-A-13	Abiotic	Dypingite	-0.16	1.09
Abio-B-18	Abiotic	Nesquehonite	-0.16	1.16
Abio-C-7	Abiotic	Nesquehonite	-0.16	1.31
Abio-C-9	Abiotic	Nesquehonite	-0.22	0.91
Abio-C-11	Abiotic	Nesquehonite	-0.16	1.28
Abio-C-12	Abiotic	Nesquehonite	-0.18	1.12
Abio-D1-8	Abiotic	Nesquehonite	-0.34	0.39
Abio-D1-18	Abiotic	Nesquehonite	-0.21	1.20
Abio-D2-8	Abiotic	Dypingite	-0.26	0.96
Abio-D2-23	Abiotic	Dypingite	-0.17	1.26
Abio-E-7	Abiotic	Nesquehonite	0.11	1.84
Abio-E-10	Abiotic	Nesquehonite	0.34	3.61
Abio-E-11	Abiotic	Nesquehonite	0.35	3.83
Abio-E-13	Abiotic	Nesquehonite	0.27	3.42
Bio-A-1	Biotic	Nesquehonite	-0.45	-1.62
Bio-A-5	Biotic	Dypingite	-0.03	1.05
Bio-A-8	Biotic	Dypingite	0.26	3.20
Bio-A-12	Biotic	Dypingite	0.30	3.78
Bio-A-15	Biotic	Dypingite	0.13	3.13
Bio-B-4	Biotic	Nesquehonite	0.08	3.11
Bio-B-6	Biotic	Nesquehonite	0.02	2.86
Bio-B-8	Biotic	Nesquehonite	-0.19	1.78
Bio-B-9	Biotic	Nesquehonite	-0.31	1.43
Bio-B-10	Biotic	Nesquehonite	-0.46	1.64
Bio-B-11	Biotic	Dypingite	-0.49	2.00

1005

1006

1007 Table 4 (continued). Calculated saturation indices for nesquehonite and dypingite from an  
 1008 experimental study (Mavromatis et al., 2012) and a natural Mg-rich wetland (Power et  
 1009 al., 2014).

<b>Mg-carbonate precipitation experiments (data from Mavromatis et al. 2012)</b>				
<b>Experiment</b>	<b>Experiment type</b>	<b>Precipitated mineral</b>	<b>Saturation index</b>	
			<b>nesquehonite</b>	<b>dypingite</b>
Bio-C-5	Biotic	Dypingite	-0.39	1.65
Bio-C-5	Biotic	Dypingite	-0.37	1.75
Bio-D-3	Biotic	Dypingite	-0.32	1.59
Bio-E-7	Biotic	Nesquehonite+Dypingite	-0.30	1.96
Bio-E-9	Biotic	Nesquehonite+Dypingite	-0.24	1.60
Bio-F-9	Biotic	Nesquehonite	-0.18	2.02
Bio-G-2	Biotic	Nesquehonite	-0.35	-1.01
Bio-G-6	Biotic	Nesquehonite	0.40	4.90
Bio-I-5	Biotic	Nesquehonite	-0.49	1.59
<b>Natural wetland (data from Power et al., 2014)</b>				
<b>Location</b>	<b>Precipitation circumstances</b>	<b>Precipitated mineral</b>	<b>Saturation index</b>	
			<b>nesquehonite</b>	<b>dypingite<sup>a</sup></b>
Atlin, North lobe of main wetland	microbial mats	Dypingite	-0.06	0.32
Atlin, South lobe of main wetland	microbial mats	Dypingite	-0.11	0.01

1010 <sup>a</sup>temperature of wetland water was 10°C, but dypingite  $K_{sp}$  used was for 25°C

1011

1012 **Figure Captions**

1013

1014 **Figure 1.** Fourier transform infrared spectroscopy (FTIR) data for selected samples. Spectra  
1015 are offset along y-axis. Intensities on the y-axis are in arbitrary units (a.u.).

1016

1017 **Figure 2.** X-ray diffraction patterns of initial nesquehonite used in the short-term (blue line)  
1018 and long-term (purple line) experiments. The location of peaks in the nesquehonite reference  
1019 pattern are indicated by black circles.

1020

1021 **Figure 3.** Scanning electron micrographs of solids. A) initial nesquehonite. B) Solid sample  
1022 after 1420 h at 5°C. C) Solid sample after 359 h at 25°C. D) Solid sample after 311 h at 35°C.

1023

1024 **Figure 4.** Fluid composition over time in all experiments. Fluid composition evolution for the  
1025 entire experimental duration: A) pH, B) Mg concentration, C) dissolved inorganic carbon  
1026 concentration (DIC). Fluid composition evolution for the first 600 h of each experiment: D)  
1027 pH, E) Mg concentration, F) DIC. Data from the 5°C, 25°C, and 35°C experiments are  
1028 indicated by gray triangles, black diamonds, and blue squares, respectively, and short- and  
1029 long-term experiments are indicated by filled and open points, respectively. Error is smaller  
1030 than symbols unless otherwise shown.

1031

1032 **Figure 5.** Logarithm of nesquehonite solubility products ( $K_{sp}^{nsq}$ ) versus reciprocal of  
1033 temperature (in Kelvin).

1034

1035 **Figure 6.** Relative stability of hydrated Mg-carbonates at 25°C. A)  $Mg^{2+}$  activity in  
1036 equilibrium with magnesite, hydromagnesite, dypingite, and nesquehonite as a function of pH.



1037 The total dissolved inorganic carbon concentration was fixed at 0.06 M, the Na concentration  
1038 was fixed at 0.16 M, and the Cl concentration was fixed at 0.10 M to reflect the conditions in  
1039 the experiments. B)  $\text{Mg}^{2+}$  activity in equilibrium with magnesite, hydromagnesite, dypingite,  
1040 and nesquehonite as a function of  $p\text{CO}_2$ . The pH was fixed at 9, Na concentration was fixed  
1041 at 0.16 M, and Cl concentration fixed at 0.10 M to reflect the conditions in the experiments.  
1042 Calculations were done using PHREEQC V3 and the modified LLNL database, as described  
1043 in section 2.4.

1044

1045 **ES-Figure 1.** X-ray diffraction patterns of reacted solids in the 5°C experiment over time.

1046 Major nesquehonite peaks are indicated by the letter “n.”

1047

1048 **ES-Figure 2.** X-ray diffraction patterns of reacted solids in the short-term 25°C experiment

1049 over time. Major nesquehonite peaks are indicated by the letter “n,” and dypingite peaks by  
1050 the letter “d.”

1051

1052 **ES-Figure 3.** X-ray diffraction patterns of reacted solids in the long-term 25°C experiment

1053 over time. Major nesquehonite peaks are indicated by the letter “n,” and dypingite peaks by  
1054 the letter “d.” The peak indicative of the dypingite stoichiometry of

1055  $[\text{Mg}_5(\text{CO}_3)_4(\text{OH})_2 \cdot 8\text{H}_2\text{O}]$  is indicated by the label “d(8H<sub>2</sub>O).” The peaks of the unidentified  
1056 dypingite-like phase are indicated by the label “d-l.” The appearance of more noise in some  
1057 patterns is attributed to lower maximum intensities for those data.

1058

1059 **ES-Figure 4.** X-ray diffraction patterns of reacted solids in the short-term 35°C experiment

1060 over time. Major nesquehonite peaks are indicated by the letter “n,” and dypingite peaks by  
1061 the letter “d.” The peak indicative of the dypingite stoichiometry of

1062  $[\text{Mg}_5(\text{CO}_3)_4(\text{OH})_2 \cdot 8\text{H}_2\text{O}]$  is indicated by the label “d(8H<sub>2</sub>O).”

1063

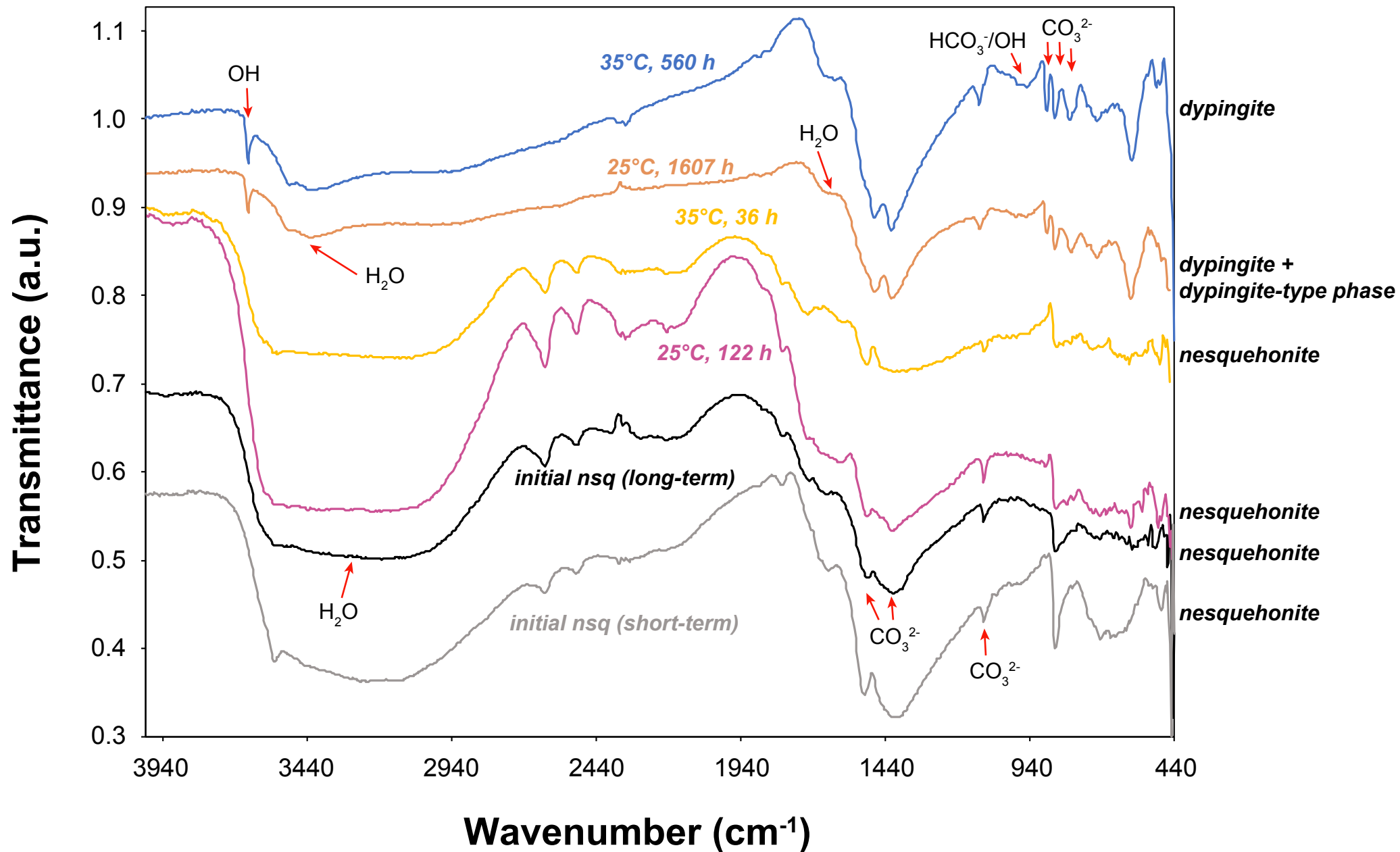
1064 **ES-Figure 5.** X-ray diffraction patterns of reacted solids in the long-term 35°C experiment

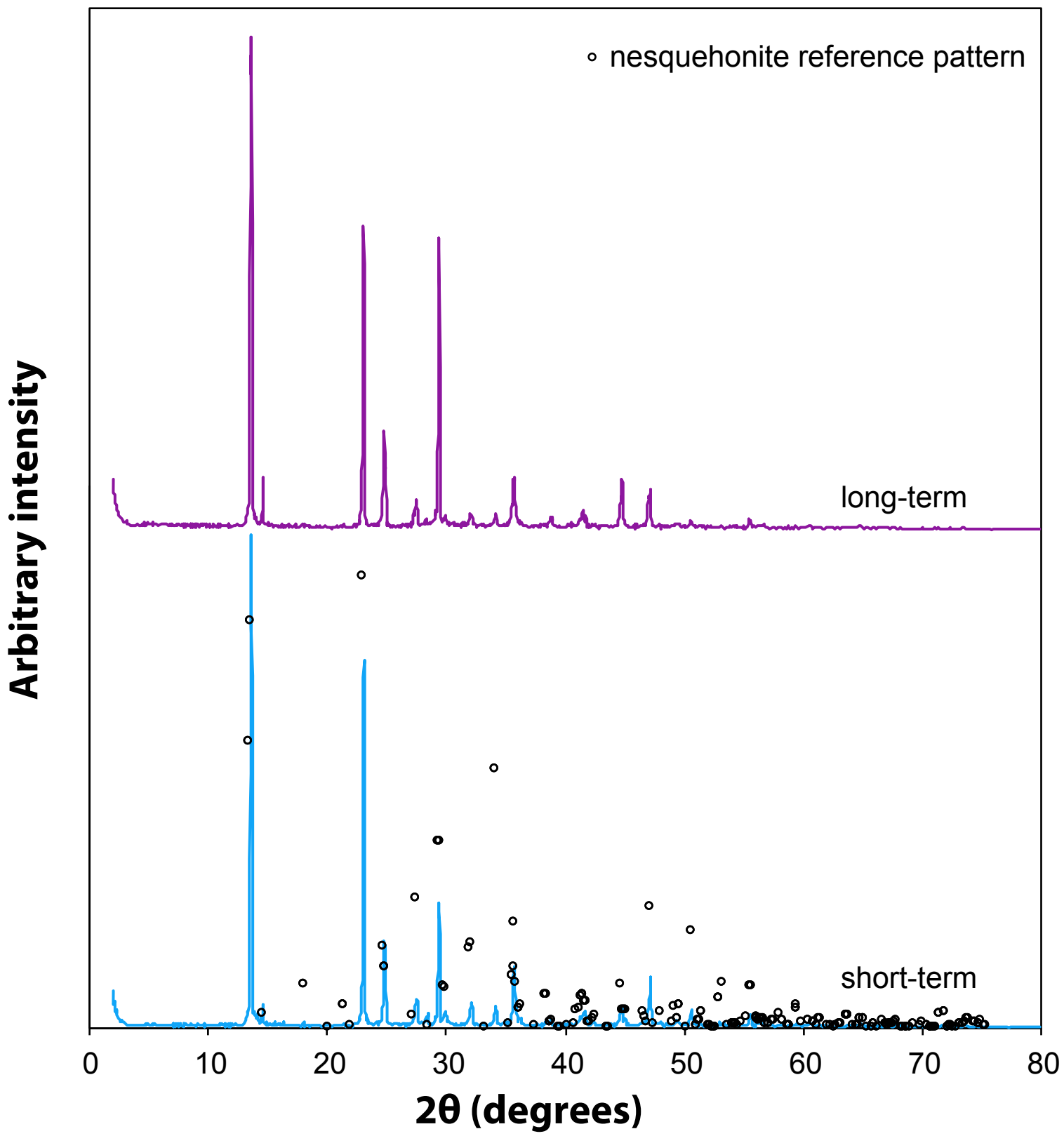
1065 over time. Major nesquehonite peaks are indicated by the letter “n,” and dypingite peaks by

1066 the letter “d.” The peak indicative of the dypingite stoichiometry of

1067  $[\text{Mg}_5(\text{CO}_3)_4(\text{OH})_2 \cdot 8\text{H}_2\text{O}]$  is indicated by the label “d(8H<sub>2</sub>O).” The appearance of more

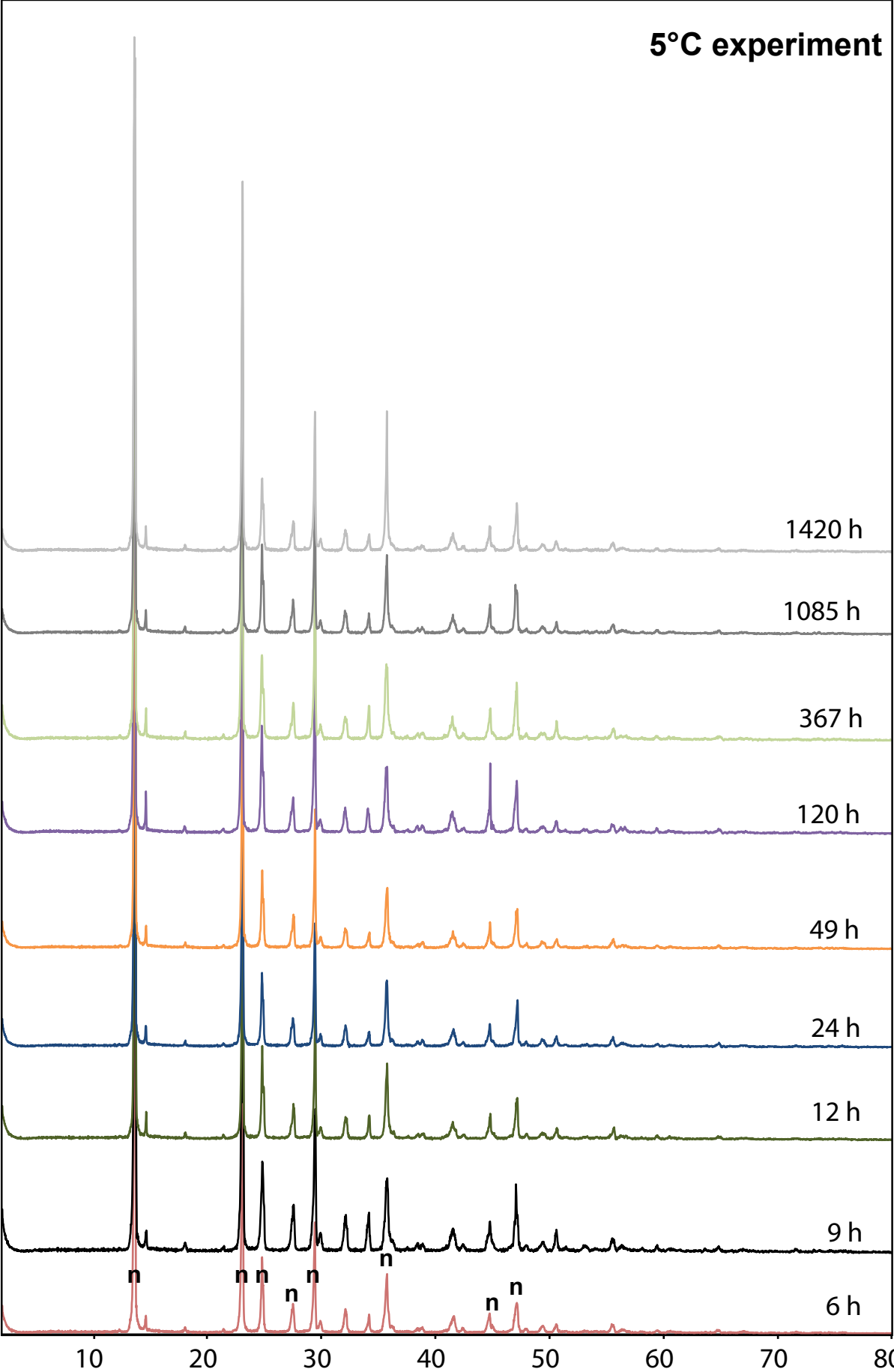
1068 noise in some patterns is attributed to lower maximum intensities for those data.





5°C experiment

Arbitrary intensity



1420 h

1085 h

367 h

120 h

49 h

24 h

12 h

9 h

6 h

10

20

30

40

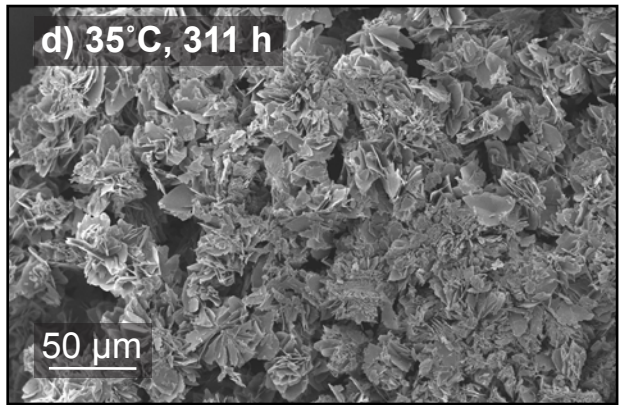
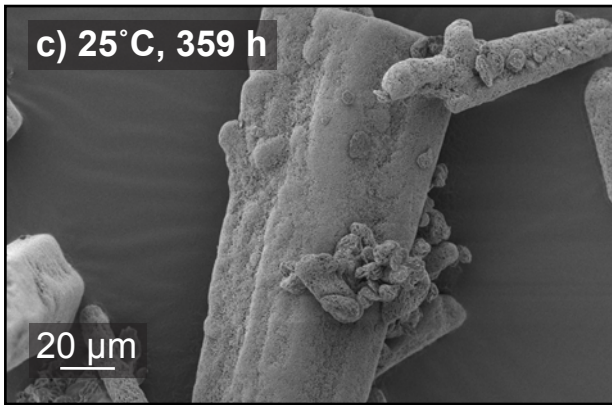
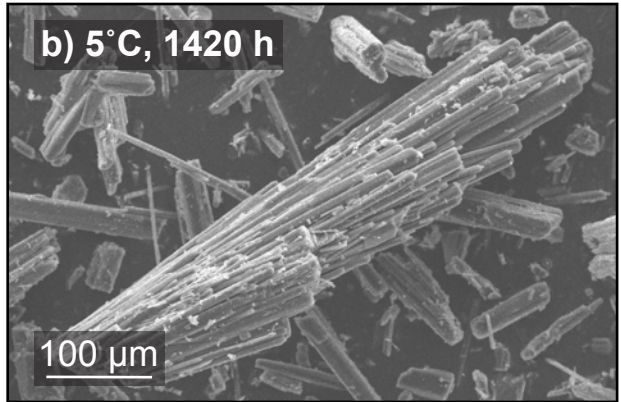
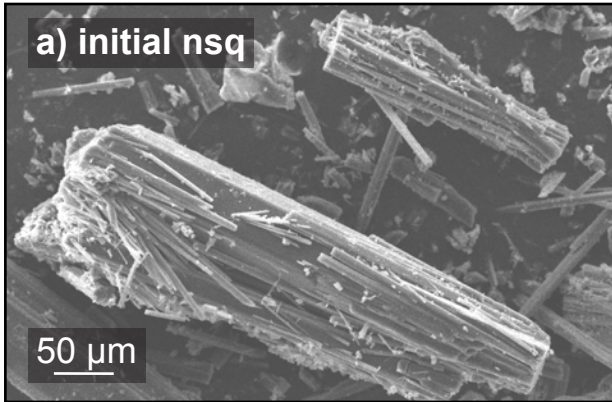
50

60

70

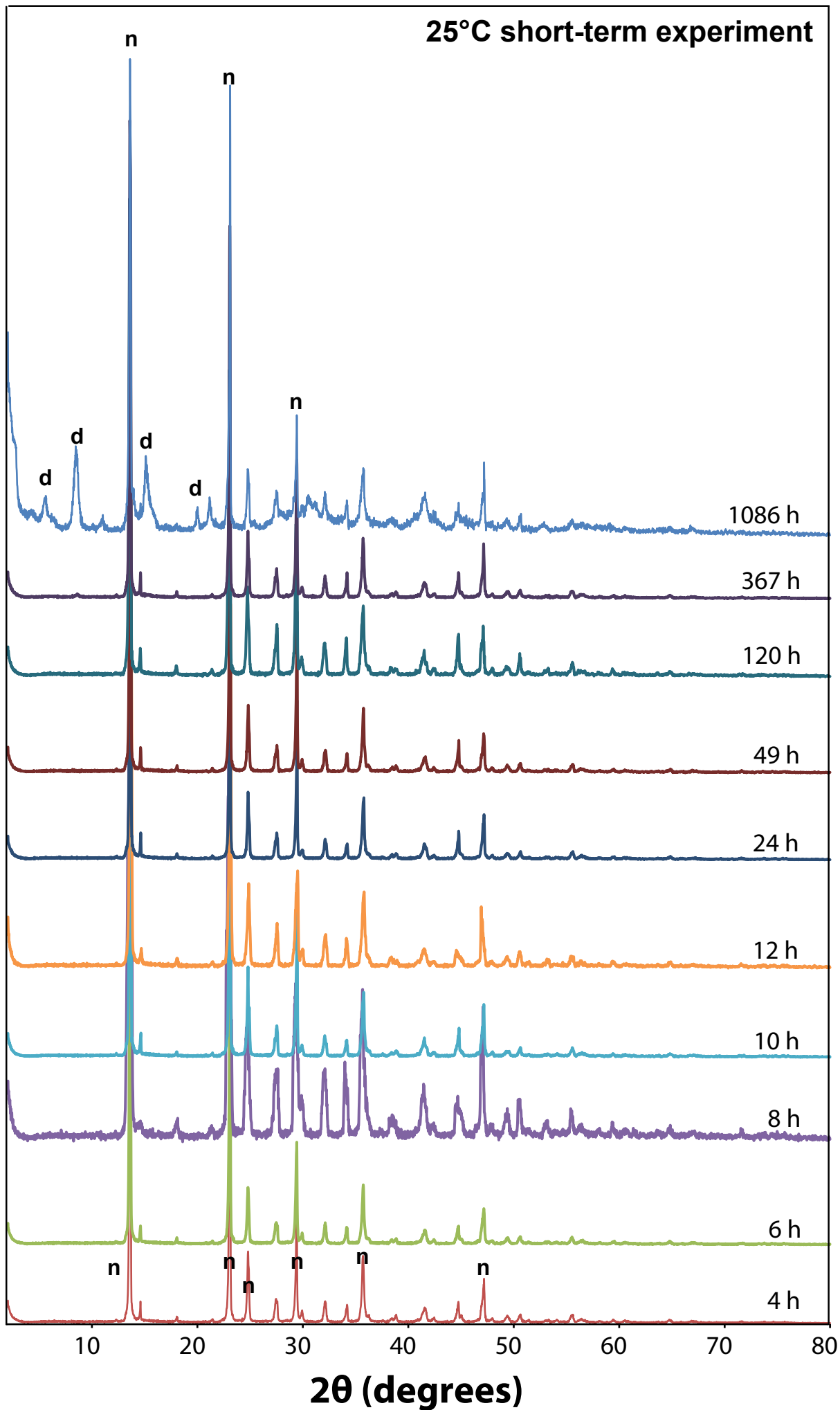
80

2θ (degrees)

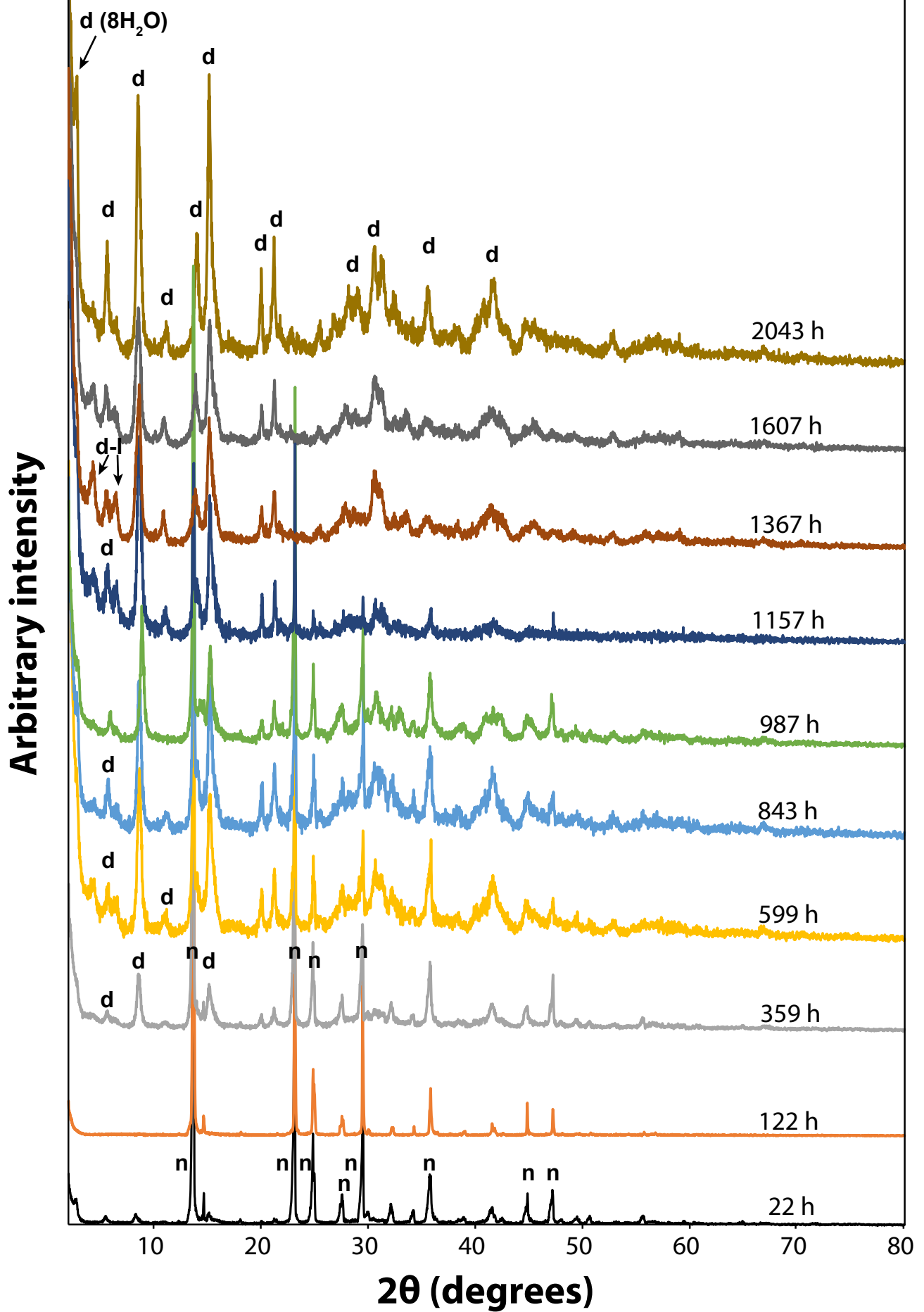


25°C short-term experiment

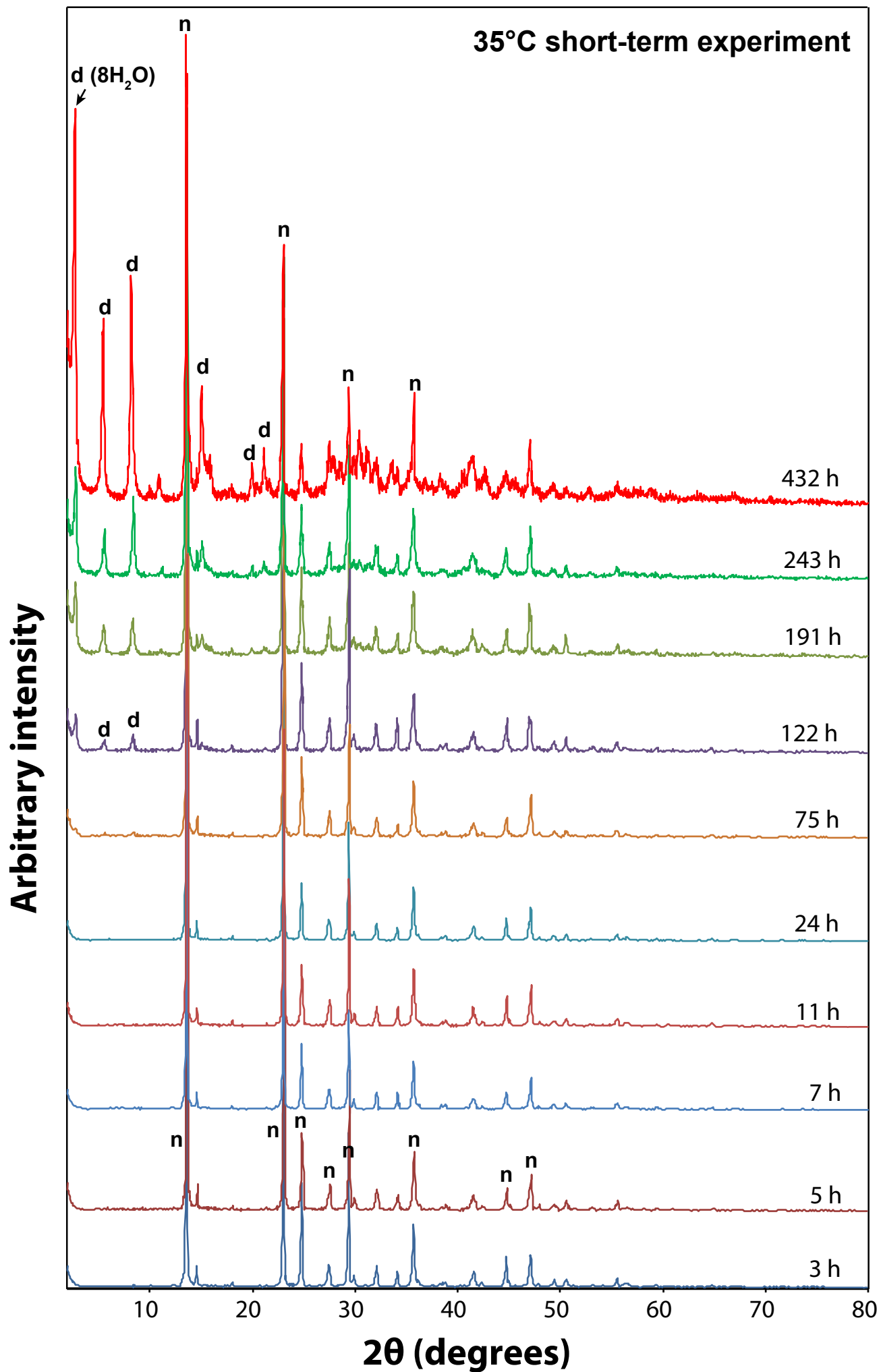
Arbitrary intensity



25°C long-term experiment

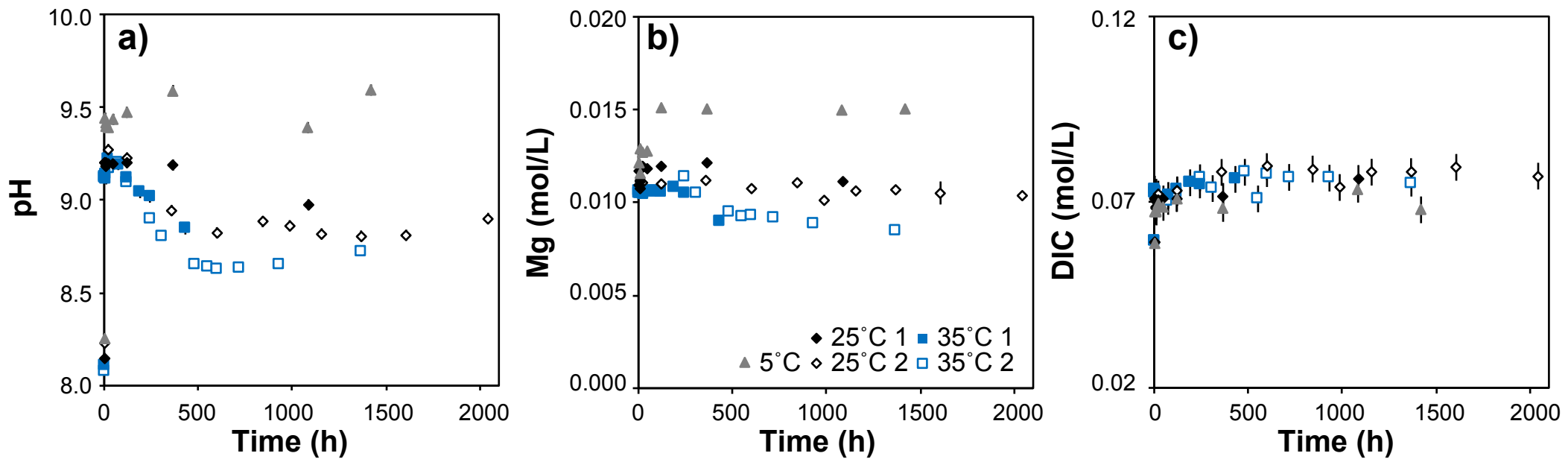








## Entirety of experimental duration



## Early time interval

